NTNU – Trondheim
Norwegian University of
Science and Technology

Cold Pressure Welding of Dissimilar Aluminum Alloys under Conditions Applicable to Hybrid Metal Extrusion & Bonding (HYB)

Erlend Andre Sandvik

Materials Science and Engineering
Submission date: June 2014
Supervisor: Øystein Grong, IMTE
Co-supervisor: Ulf Roar Aakenes, HyBond AS / Enoco AS

Norwegian University of Science and Technology
Department of Materials Science and Engineering

Abstract

Traditional solid-state welding methods mainly focuses on joining of similar materials. But with the increased interest in multi-material constructions more research is needed on joining of dissimilar materials. In the present thesis dedicated cold pressure welding experiments with dissimilar aluminum alloys have been performed. The alloy combinations investigated were cold-deformed AA5183 and soft-annealed AA5183 (Series II) and cold-deformed AA5183 and commercial purity AA1050 (Series III). In both series metallic bonding is initiated when a critical value of the compressive plastic strain is reached. A small increase in the strain beyond this threshold leads to full metallic bonding. In Series II the soft-annealed AA5183 material rapidly work-hardens during upsetting until the pressure at the contact section becomes equal to that of the cold-deformed AA5183 material. At this point the two interfaces start to mate before the bonding process eventually commences. In Series III the soft commercial purity AA1050 material is unable to work-harden to any great extent. Instead, the cold-deformed AA5183 material starts to penetrate the soft AA1050 wire. This leads to build-up of an internal extrusion pressure approaching that of the cold-deformed AA5183 material. The local material flow pattern occurring at the interface will then determine the actual surface exposure at which full metallic bonding is achieved.

Sammendrag

Tradisjonelt har solid-state sveisemetoder hovedsakelig fokusert på sammenføyning av like materialer. En økende interesse for flermaterielle konstruksjoner gjør det nødvendig med mer forskning på sammenføyning av ulike materialer. I denne avhandling er det blitt utført eksperimenter der ulike aluminiumslegeringer er sammenføyd ved bruk av kaldsveising. Legeringskombinasjonene som ble undersøkt var kald-deformert AA5183 og mykglødet AA5183 (Series II) og kald-deformert AA5183 og kommersielt ren AA1050 (Series III). I begge seriene initieres metallbinding når en kritisk tøyningsverdi oppnås. En liten økning i den plastiske deformasjonen utover denne verdien fører til full metallisk binding. I Series II arbeidsherder den mykglødede AA5183 raskt under stukingen inntil trykket ved kontaktflaten blir lik flytespenningen i den tilhørende kald-deformerte AA5183 legeringen. Ved dette stadiet vil de to kontaktflatene presses sammen før bindingsprosessen til slutt starter. I Series III er den myke kommersielt rene AA1050 legeringen ikke i stand til å arbeidsherde i noen særlig grad. Istedenfor vil den kald-deformerte AA5183 legeringen penetrere den myke AA1050-tråden. Dette fører til oppbygning av et indre ekstruderingstrykk som nærmer seg flytespenningen i den tilhørende kald-deformerte AA5183 legeringen. Det lokale flytmønsteret som oppstår ved grenseflaten vil da bestemme overflateeksponeringen som kreves for å oppnå full metallisk binding.

Preface

This work has been carried out at the Norwegian University of Science and Technology (NTNU), Department of Materials Science and Engineering over a period of twenty weeks from January 2014 to June 2014.

The work is done as a part of the Hybrid Metal Extrusion and Bonding (HYB) development project at NTNU. This is an ongoing project with the goal to industrialize a new solid state joining process for aluminum in which a filler wire is continuously squeezed into the groove between the two aluminum plates to be joined under high pressure to achieve metallic bonding. Although just conventional cold pressure welding has been carried out in the present thesis work, the results reported here are deemed to provide a basis for understanding the bonding mechanisms in the HYB case as well.

Acknowledgments

I would like to express my sincere gratitude to my supervisor Prof. Øystein Grong for his constructive guidance, encouragement and countless discussions. I would also like to thank Trygve Schanche and Yingda Yu for their help in the laboratory.

Contents

Abstract i

Sammendrag iii

Preface v

Acknowledgments vii

List of Tables xi

List of Figures xv

1. Introduction 1

2. Theory 3
- 2.1. The mechanisms of cold bonding 3
  - 2.1.1. Metallic bonding 3
  - 2.1.2. Importance of plastic deformation 3
  - 2.1.3. Surface expansion and exposure 5
  - 2.1.4. Surface preparation and nozzle formation in brittle oxide layers 7
  - 2.1.5. Relationship between P_e and Y 8
- 2.2. Cold pressure welding, CPW 9
  - 2.2.1. Formation of flash 9
  - 2.2.2. CPW of similar aluminum alloys 10
- 2.3. Cold bonding of dissimilar materials 10

3. Experimental procedure 12
- 3.1. Base materials 12
- 3.2. Series I: Soft annealing experiments 12
  - 3.2.1. Light microscopy 12
  - 3.2.2. Hardness measurements 13
- 3.3. Series II & III: Cold pressure welding experiments 13
  - 3.3.1. Welding equipment 13
  - 3.3.2. Welding experiments 14
  - 3.3.3. Light and scanning electron microscopy 15
  - 3.3.4. Hardness measurements 16
  - 3.3.5. Additional testing of samples from Series III 16

4. Results 17
- 4.1. Series I: Soft-annealing experiments 17
  - 4.1.1. Microstructure of cold-deformed and soft-annealed samples 17
  - 4.1.2. Hardness reduction during soft-annealing 18

4.2. Series II & III: Cold pressure welding experiments 18
4.2.1. Microstructure and flow pattern within the weld zone 18
4.2.2. Hardness distribution across the weld zones 20
4.3. Bond strength of cold pressure welds 22
4.4. Fracture surface appearance of broken bend test specimens 23

5. Discussion 25
5.1. Contact pressure build-up during upsetting 25
5.2. Steepness of hardness gradient across the weld zone 27
5.3. Material flow pattern during upsetting 30
5.4. Origin of dark demarcation line at joint interface 33
5.5. Statistical analysis of the bend test results 36
5.5.1. Cumulative probability for bonding 36
5.5.2. Surface expansion and surface exposure of the bulk materials . . . 38
5.6. Cold bonding mechanism in dissimilar aluminum joints 38

6. Conclusions 41

References 42

Appendix 45

A. Soft-annealing experiments 45

List of Tables

3.1. Chemical composition of the alloys used in the experiments. 12
3.2. A list of the different alloy combinations used in the experiments. 14
5.1. Calculated values for the probability of bonding during CPW of cold-deformed AA5183 and soft-annealed AA5183 within different strain intervals (Series II). 36
5.2. Calculated values for the probability of bonding during CPW of cold-deformed AA5183 and commercial purity AA1050 within different strain intervals (Series III). 36
5.3. Nominal strain required to achieve bonding in Series II and III at different levels of probability. 37
5.4. Calculated values for the surface expansion and surface exposure needed to achieve bond initiation at $P(X \leq x) = 0.05$ (left values) and full bonding $P(X \leq x) = 0.995$ (right values), respectively in Series II and III. 38

List of Figures

2.1. Sketch showing the aluminum atom. 3
2.2. Illustrations showing how plastic deformation changes the surface topography. From [17]. 4
2.3. Illustrations showing how the oxide layer breaks up by plastic deformation and metal extrudes through the cracks to form bonding. From [17]. . . . 4
2.4. Illustration of a cross section of a plastically deformed sample. 5
2.5. Illustration of joining of two plates by rolling. 6
2.6. Illustration of the "nozzle cracks" formed in the oxide layer. 7
2.7. Illustration of the problem and definition of the "nozzle crack" parameters. 7
2.8. Extrusion pressure as a function of surface exposure. From [6]. 8
2.9. The process of cold pressure welding by the use of upsetting. From [17]. . 9
2.10. Cold pressure welding of ⌀1.6 mm wire of AA5183; (a) Optical microscope picture of the microstructure showing the flow pattern of a welded sample, (b) Hardness profile across the deformation zone rotated 90°. From [17]. 10
2.11. Illustration of joining of two dissimilar plate materials by rolling. 10
3.1. Sketch showing how the hardness measurements were performed in Series I. 13
3.2. Photograph of the manually operated CPW machine used in the experiments; (a) side view, (b) top view. 13
3.3. Sketches showing how the lengths before and after welding were measured. 14
3.4. Sketches showing the different stages of the bend test. 15
3.5. Photograph showing examples of successful bonding (top) and a non-successful bonding (bottom). 15
3.6. Sketch showing how the hardness was measured on the cold-welded samples (Series II and III). 16
4.1. Optical microscope picture of the microstructure of AA5183 (a) before and (b) after heat treatment at 400°C. 17
4.2. Graphical representation of the measured hardness drop in the cold-deformed AA5183 alloy following soft-annealing at different temperatures. The error bars in the graph represent standard deviation of the hardness measurements. 18
4.3. Optical microscope collage of the anodized weld zone showing the microstructure and flow pattern within the cold-deformed AA5183 (top) and the soft-annealed AA5183 (bottom) materials. 19
4.4. Optical microscope collage of the anodized weld zone showing the microstructure and flow pattern within the cold-deformed AA5183 (top) and the commercial purity AA1050 (bottom) materials. 19
4.5. Optical microscope collage of the anodized weld zone showing the microstructure and flow pattern within the cold-deformed AA5183 (top) and commercial purity AA1050 (bottom) materials in the absence of polarized light. 20

4.6. Graphical representation of the measured hardness distribution across the weld zone for (a) cold-deformed AA5183 and soft-annealed AA5183 (Series II) and (b) cold-deformed AA5183 and commercial purity AA1050 (Series III). Note the difference in the hardness scale between Series II and III. The error bars in the graphs represent the standard deviation of the hardness measurements. 21
4.7. Graphical representations of the bend test results obtained in (a) Series II and (b) Series III. In these graphs the final outcome of the bend testing (i.e. bonding or no bonding) is plotted versus the nominal strain e_n, as calculated from Equation 4.1. A value of 1 means bonding, whereas a value of 0 means no bonding. 22
4.8. SEM fractographs of broken bend test specimens from (a-b) Series II and (c-d) Series III. 24
5.1. Schematic representation of the flow stress σ_0 profiles before and after upsetting during CPW of two dissimilar alloys. 25
5.2. Experimental stress-strain curve for AA5083. The re-drawing is based on data from Ref. [20]. 26
5.3. Experimental stress-strain curves for AA5083 and AA1050 superimposed in the same diagram. The re-drawing is based on data from Refs. [14, 20]. 27
5.4. Optical microscope collage showing the micro-hardness imprints taken across the weld zone of cold deformed AA5183 (top) and commercial purity AA1050 (bottom). 28
5.5. Results from micro-hardness measurements carried out across the weld zone of cold-deformed AA5183 and commercial purity AA1050; (a) individual hardness profiles for all three locations indicated in Figure 5.4, (b) average hardness profile across the weld zone. The error bar in the lower graph represents the standard deviation of the hardness measurements. . 29
5.6. Graphical representation of the combined macro- and micro-hardness data for cold-deformed AA5183 and commercial purity AA1050. The error bar in the graph represents the standard deviation of the hardness measurements. 30
5.7. Graphical representations of the actual change of length of the softest specimen compared to the total measured change of length during upsetting of (a) cold-deformed AA5183 and soft-annealed AA5183 (Series II) and (b) cold-deformed AA5183 and commercial purity AA1050 (Series III). 31
5.8. Schematic illustrations of the assumed material flow pattern during CPW of (a) cold-deformed AA5183 and soft-annealed AA5183, (b) cold-deformed AA5183 and commercial purity AA1050. The arrows in the sketches indicate the magnitude and direction of the material flow at the different locations. 32
5.9. Optical microscope collage of the pre-anodized weld zone of cold-deformed AA5183 (top) and commercial purity AA1050 (bottom). 33
5.10. Optical microscope picture of the weld zone of cold-deformed AA5183 (top) and commercial purity AA1050 (bottom) as viewed in the DIC mode. 34

5.11. Optical microscope collage of the anodized weld zone of cold-deformed AA5183 (top) and commercial purity AA1050 (bottom) as viewed in normal light. 34
5.12. Optical microscope collage of the anodized weld zone of cold deformed AA5183 (top) and commercial purity AA1050 (bottom) as viewed in polarized light. 35
5.13. Optical microscope picture of the anodized weld zone of cold-deformed AA5183 (top) and commercial purity AA1050 (bottom) as viewed in the DIC mode. 35
5.14. Plots showing the cumulative probability of bonding as a function of nominal strain for (a) Series II and (b) Series III. 37
5.15. Sketch showing how the surface expansion and the surface exposure can be calculated from measurements of the flash thickness Δx. 38
5.16. Schematic drawing of the contact section, as viewed normal to the wire length direction. In this case A_0 is the nominal wire cross section, while ΔA^* is the new interfacial area and ΔA is the total surface area, respectively, which form during upsetting. 39
5.17. Graphical representation of Equation 5.8 showing the evaluation of Y^* with e_n for different z-values. 40
A.1. Optical microscope pictures of the microstructure of AA5183 (a) before heat treatment (b) after heat treatment at 100°C (c) after heat treatment at 200°C (d) after heat treatment at 300°C (e) after heat treatment at 400°C. 45

1. Introduction

The interest in cold welding as a joining method for metals has seen to increase in recent years, mainly with regard to aluminum. Traditional fusion welding, developed for ferrous metals (e.g. MIG and TIG), has never been an optimal method for aluminum. With fusion welding being based on the principles of melting both base and filler metals, an unwanted consequence occurs for aluminum. Ferrous metals and alloys are usually engineered in such a way that no or limited decrease in properties is caused by the process of welding. However, melting aluminum can cause a decrease in the yield stress by up to as much as 50% [1, 2]. To compensate this, manufacturers double the sections of the construction, which, in turn, makes it twice as heavy and expensive, and less likely to be a competitor to steel. Due to this, several methods have been developed since the original discovery of cold bonding in 1724 [3]. Although methods of both high and low process temperatures have been developed, only the low temperature methods being used for metallic materials will be discussed here, as they do not degrade the properties due to excessive heating.

Cold roll bonding (CRB) is a process where plates or sheets of metal are stacked and passed through a rolling mill [4]. The process is repeated until solid state bonding has occurred. A severe plastic deformation is required due to the presence of contaminant layers on the surface. This causes the layer to break up and virgin metal to be extruded through the newly created cracks [5]. It is discovered that a surface exposure of around 60-70% is required to obtain a weld strength close to that of the base material [6].

Another process is cut welding (CW) [7]. Because of the problems caused by the contaminant layer, this process was developed as an alternative to CRB - where the contaminant layer calls for the use of severe plastic deformation. To deal with the contaminant layer, this process cuts it off entirely. In one slick motion, the surface layer of each piece is sheared off simultaneously as the pieces are joined together. Once they are aligned, they are upset by a punch. Unlike CRB, only about 30% of the weld strength is obtainable due to problems associated with the control of the process [8].

The last process of interest here is cold pressure welding (CPW) [9]. Among the different CPW methods, only cold pressure butt welding will be covered, which in the following is referred to as CPW. Its main use is for joining of rods of different sizes, typically from 1 to 30 mm in diameter [10]. The process is performed by positioning the two ends of the rods against each other, while applying a force along the axis of the rods. A high enough force will cause upsetting so that the contaminant layers are squeezed out and form a flash. The weld strength increases with the degree of plastic deformation and full metallic bonding is achieved above a critical level [11].

Still, one crucial problem remains unsolved and needs to be addressed. These three methods are all tested and developed based on joining of similar materials. With an increasing demand for hybrid structures, there is a growing need for new joining methods for dissimilar materials. Thus, it is important to understand and further develop existing welding methods such as cold welding. Even though there is a lack of knowledge in this field, previous research has shown that joining of dissimilar materials through the use of CRB is possible [4, 12, 13]. Examples of successful metal combinations are Al-Cu, Al-Fe and Al-Ti. These metals cannot be joined together by means of traditional fusion welding, which makes cold welding a strong choice. Among the three previously mentioned methods, CPW is the most interesting solid state joining method to be further investigated. This is due to the previous success of using CPW to unravel the conditions under which cold bonding takes place in aluminum at room temperature in the presences of hydrated surface oxide and other contaminants at the interface [14, 15]. In addition, it has been shown that CPW keeps the microstructure intact even after joining of severely plastically deformed aluminum [16].

In this thesis, attempts will be made to unravel the conditions under which cold bonding takes place in CPW of dissimilar aluminum alloys. The alloys used are AA1050 and AA5183, where the latter will be welded both in the soft-annealed and cold-deformed state. The bond strength is evaluated by performing CPW on a combination of said alloys, followed by a simple bend testing. The subsequent metallographic investigation, involving hardness measurements, light microscope and scanning electron microscope, are performed to document the microstructure of both bonded and fractured samples and to shed new light upon the bonding mechanisms involved.

2. Theory

In this chapter the fundamental known mechanisms behind the process of cold welding of aluminum will be briefly discussed. In addition, a deeper look into the cold roll bonding (CRB) and the cold pressure welding (CPW) processes will be provided.

2.1. The mechanisms of cold bonding

2.1.1. Metallic bonding

Metallic bonding is the ultimate goal of cold welding. As the name indicates it is an atom bonding mechanism for metals. All metallic elements have an electropositive core. When surrounded by their own kind, they will donate their valence electrons to form a "sea". This sea surrounds the metal cores from which they came. In this case the metal is aluminum. Aluminum donates three valence electrons per atom to the sea, as seen in Figure 2.1. By doing so, the core and remaining electrons have a positive charge of three. A mutual attraction between these positively charged ion cores and the negatively charged electron sea produces a strong metallic bonding. It is the freely moving valence electrons in the sea that contributes to the pure metals' good electrical conductivity. In addition, the relatively high Young's modulus is caused by the strength of the metallic bonding, and the good ductility by the non-directional behavior of the bonding.

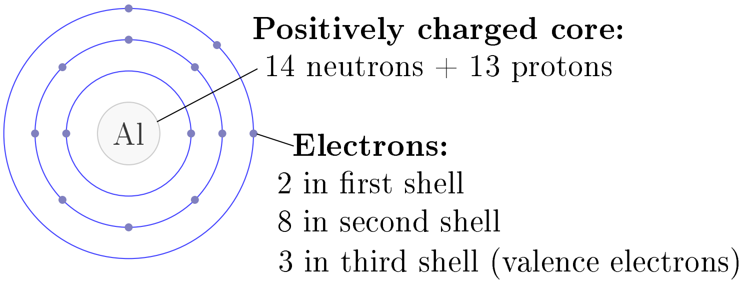

Figure 2.1: Sketch showing the aluminum atom.

2.1.2. Importance of plastic deformation

It is crucial that the aluminum atoms are in close proximity to one another for bonding to occur. However, when two pieces of the same metal are put together, their surfaces are not fully in contact. On a microscopic scale the surfaces are rough, full of grooves and hills. An uneven surface causes the contact zone to be limited to where the highest points meet. Thus, bonding can only occur on a fraction of the total surface area. By applying force, the pressure on these few points will start to exceed the yield strength. Yielding will then increase the contact area as illustrated in Figure 2.2. The overlapping deformation zones in the rightmost figure are caused by the deformation of the surface. They form just beneath the surface and contribute to reducing the contact area needed to reach base material strength by introducing work hardening.

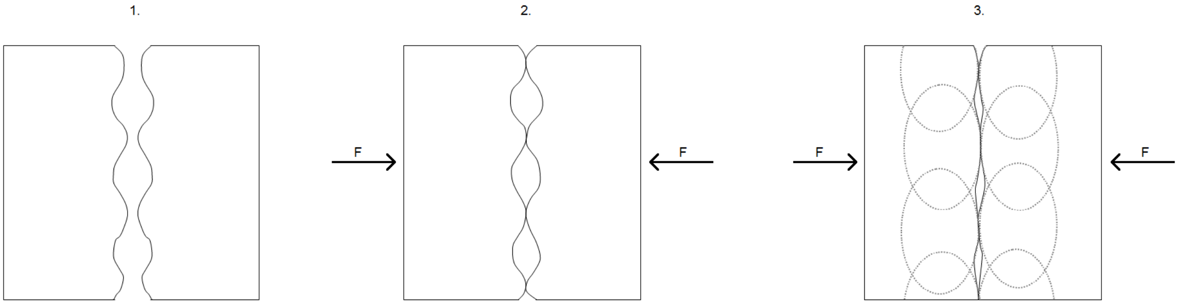

Figure 2.2: Illustrations showing how plastic deformation changes the surface topography. From [17].

There is, however, one minor inconvenience. In natural condition no metal is clean. Surface layers of oxides, oils and other contaminants are always present. These layers work as a barrier between the virgin metal cores, preventing metallic bonding. To obtain bonding, one must break these layers apart. There are two ways of doing this. For thick oxide layers the plastic deformation will break up the brittle oxide. This, in turn, opens up cracks in the oxide where virgin metal can extrude through [6]. This is illustrated in Figure 2.3. For thin oxide layers the mechanisms are slightly different. Oxides become more ductile with reduced thickness [4, 6]. Thus, the plastic deformation will no longer break it apart. Instead, it will stretch the layer until it is so thin that it becomes negligible. Once reaching that stage, direct virgin metal contact will happen and metallic bonding can occur.

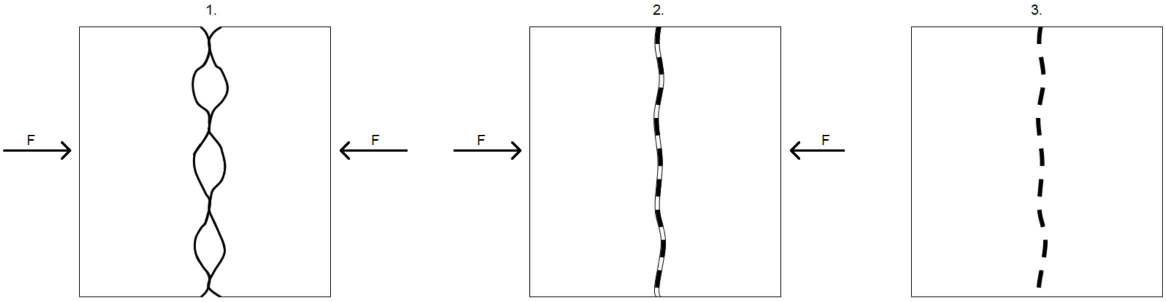

Figure 2.3: Illustrations showing how the oxide layer breaks up by plastic deformation and metal extrudes through the cracks to form bonding. From [17].

2.1.3. Surface expansion and exposure

One method to calculate the plastic deformation and its effect on the oxide layer is to introduce the following parameters:

Surface expansion:

$$X = \frac{A_1 - A_0}{A_0} = \frac{A_1}{A_0} - 1 \tag{2.1}$$

Surface exposure:

$$Y = \frac{A_1 - A_0}{A_1} = 1 - \frac{A_0}{A_1} \tag{2.2}$$

Surface expansion is as simple as it sounds. It measures the increase - or expansion - of the contact area between the two joined plastically deformed units. Surface exposure is slightly trickier to explain. By assuming that the surface oxide is completely brittle (i.e. no thinning of the oxide occurs during the plastic deformation), the surface exposure will be a measure of the area fraction of the new oxide-free surface being created during the plastic deformation. This follows from the analysis below:

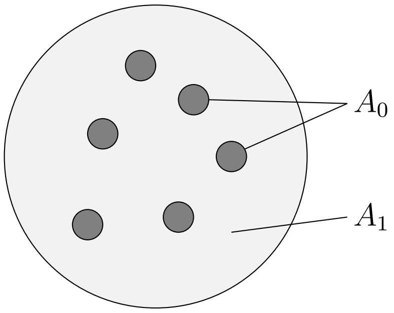

Figure 2.4: Illustration of a cross section of a plastically deformed sample.

It follows from Figure 2.4 that A_0/A_1 is the area fraction of the original surface covered by oxide, whereas $1 - A_0/A_1$ is the area fraction of the new oxide-free surface being created during the plastic deformation. In addition, both X and Y can be related to the plastic strain ϵ_p being imposed on the material during the deformation process, taking [18]:

$$\epsilon_p = ln(\frac{A_1}{A_0}) \tag{2.3}$$

A combination of Equations 2.1-2.3 then gives:

$$\epsilon_p = ln(X+1) \tag{2.4}$$

and

$$\epsilon_p = ln(\frac{1}{1-Y}) \tag{2.5}$$

Specifically, in rolling of plates the A_1/A_0 ratio can be related to the corresponding reduction in thickness h_0/h_1, as can be seen from Figure 2.5.

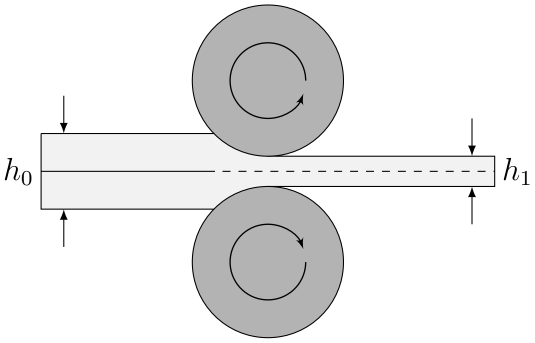

Figure 2.5: Illustration of joining of two plates by rolling.

Since the volume is conserved during the rolling process, the following relationship holds:

$$A_0 \cdot h_0 = A_1 \cdot h_1 \tag{2.6}$$

from which

$$\frac{A_1}{A_0} = \frac{h_0}{h_1} \tag{2.7}$$

and

$$\epsilon_p = ln(\frac{A_1}{A_0}) = ln(\frac{h_0}{h_1}) \tag{2.8}$$

It follows that there is a direct relationship between the imposed plastic strain and the surface expansion during rolling. As a matter of fact, the same is also true for other cold welding processes as well (to be discussed later).

2.1.4. Surface preparation and nozzle formation in brittle oxide layers

As already stated, the oxide layer will in many cases not be hard and brittle, but instead thin and ductile. To obtain a brittle oxide layer, the surface needs to be altered [6]. One method used in cold roll bonding is scratch-brushing of the surface. By scratching the surface it is possible to obtain areas of thick brittle material covered by oxide. This, in turn, makes it easier to break-up the oxide layer, allowing for virgin metal to be extruded through the newly formed cracks. By simplifying the concept, the cracks can be seen as tiny nozzles going through the oxide layer. This is illustrated in Figure 2.6.

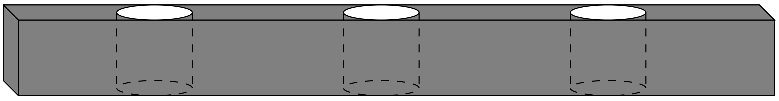

Figure 2.6: Illustration of the "nozzle cracks" formed in the oxide layer.

For extrusion to happen through the nozzles, the extrusion pressure P_e limit needs to be reached. At first glance this may seem easy due to the incredibly short crack length L. But by examining the problem further along the lines indicated in Figure 2.7, this can be proved to be a formidable task.

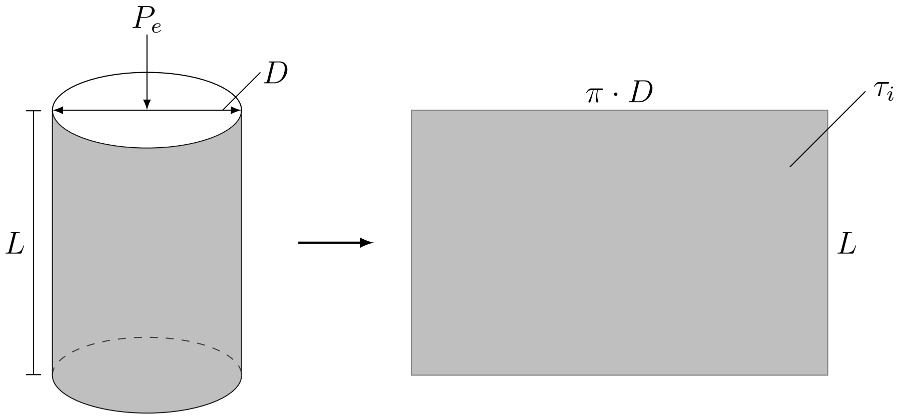

Figure 2.7: Illustration of the problem and definition of the "nozzle crack" parameters.

From Figure 2.7 the following pressure balance can be derived:

$$P_e \cdot \frac{\pi D^2}{4} = \pi D \cdot L \cdot \tau_i \tag{2.9}$$

where τ_i is the yield strength of the material in pure shear. By invoking the von Mises' yield criterion, τ_i can be related to the macroscopic flow stress σ_0 of the same material through the well-known relationship:

$$\tau_i = \frac{\sigma_0}{\sqrt{3}} \tag{2.10}$$

A combination of Equations 2.9 and 2.10 then leads to the following expression for the extrusion pressure, P_e:

$$P_e = \frac{4}{\sqrt{3}}\sigma_0 \cdot \frac{L}{D} \tag{2.11}$$

Because the diameter D of the cracks in the surface oxide layer acting as extrusion channels for the pure metal is very small (of the order of nanometers), the extrusion pressure needed to initiate the flow is still very high. This point will be further elaborated and discussed below.

2.1.5. Relationship between P_e and Y.

As shown in Equation 2.11, the pressure required for extrusion through cracks in brittle oxide layer will be a function of the crack width D. Because the crack width can be directly related to the surface exposure, a relationship between P_e and Y is to be expected and be calculated as illustrated in Figure 2.8:

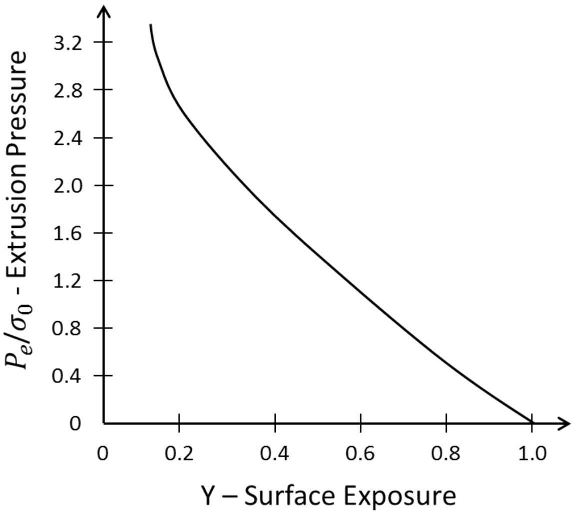

Figure 2.8: Extrusion pressure as a function of surface exposure. From [6].

In the example given in Figure 2.8 the material used was cold rolled Al 99.5. From this it is evident that an increased surface exposure (i.e. larger width of the nozzles) will reduce the amount of pressure required for extrusion. At low levels of plastic deformation the metal surface is covered by solid oxide not yet cracked. Beyond a critical plastic deformation the oxide starts to crack, which in this case is just below $Y = 0.2$. Now the metal can be extruded through the nozzles, although the pressure required is very high. The extrusion pressure decreases as more oxide is broken apart, until the maximum limit represented by $Y = 1$ is reached. At this point all oxide has been removed and no pressure is required due to the direct contact between the two virgin metal surfaces.

2.2. Cold pressure welding, CPW

The solid state joining process of particular interest here is cold pressure welding (CPW). It shares most of the basic mechanisms with the previously mentioned cold roll bonding, though there are some important differences. The most striking difference is how the two processes handle the oxide layer problem.

2.2.1. Formation of flash

Unlike CRB, CPW does not break-up the brittle oxide layer to allow virgin metal to extrude through it. Nor does it matter whether the oxide is brittle or ductile. The way CPW handles the contaminant layer present at the surface is to simply squeeze it out and into the surrounding collar in the form of flash. This is done by upsetting the two pieces of metal against each other in such a way that the only route for the oxide to move is out from the center and towards the periphery. An illustration of this process is shown in Figure 2.9.

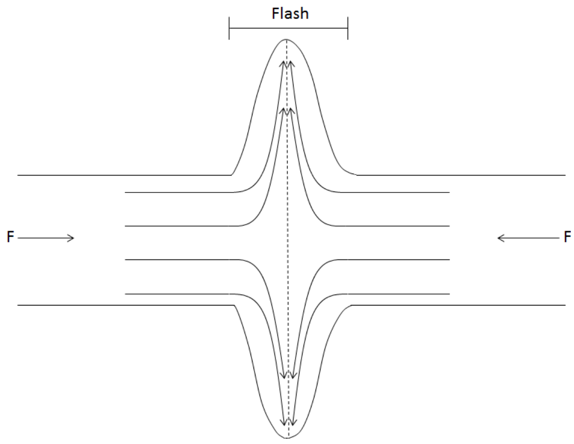

Figure 2.9: The process of cold pressure welding by the use of upsetting. From [17].

By squeezing out most, if not all, of the oxide layer, the remaining surface will contain virgin metal free of any contaminant. Metallic bonding is then easily obtained. This occurs when the surface exposure Y typically exceeds 0.9, which is a requirement for good metallic bonding [4, 6].

2.2.2. CPW of similar aluminum alloys

An example of a successful CPW of two ∅1.6 mm wires of AA5183 is shown in Figure 2.10 (a). From the flow pattern the metal is seen to bend outwards when approaching the weld zone, while the weld zone itself is completely recrystallized containing small grains. Figure 2.10 (b) further shows that the hardness increases within the weld zone. This is an indication of work hardening during the welding process. It also indicates that the joint is actually stronger than the base material. However, what is truly extraordinary is the fact that CPW is possible on an Al-Mg alloy with hardness as high as 150 VPN, and that the welding process leads to a further increase in the hardness up to 170 VPN in the joining zone due to work hardening.

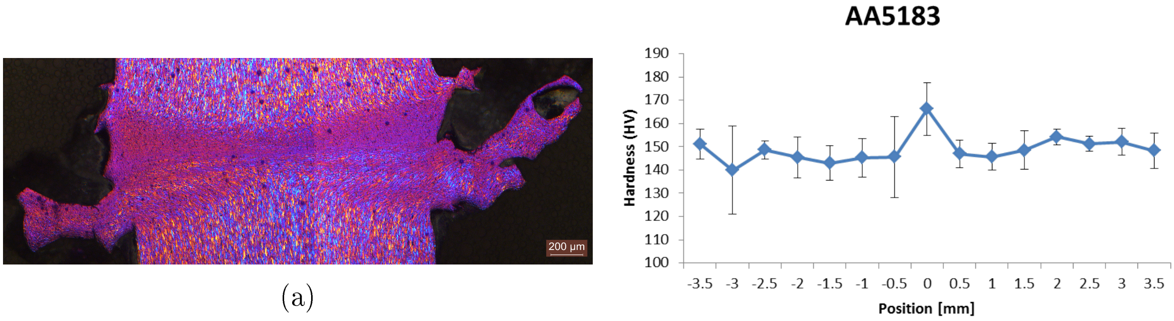

(a)

(b)

Figure 2.10: Cold pressure welding of ∅1.6 mm wire of AA5183; (a) Optical microscope picture of the microstructure showing the flow pattern of a welded sample, (b) Hardness profile across the deformation zone rotated 90°. From [17].

2.3. Cold bonding of dissimilar materials

When it comes to cold bonding of dissimilar materials very little information is available in the scientific literature. However, some research have been done by Zhang and Bay [12] on cold roll bonding.

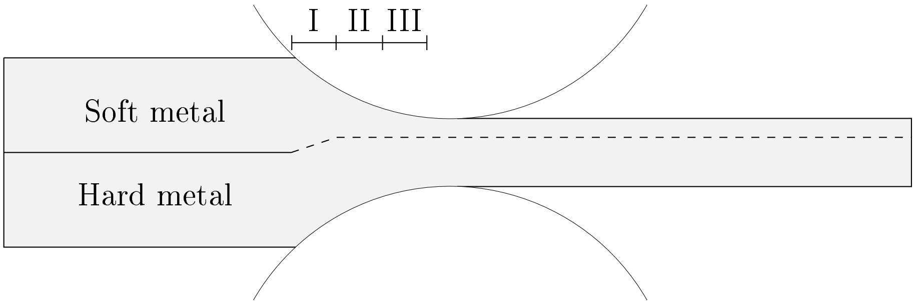

Figure 2.11: Illustration of joining of two dissimilar plate materials by rolling.

Figure 2.11 illustrates the mechanisms behind CRB of two dissimilar metals with different flow stresses. As can be seen from the illustration, three distinct zones are observed. In zone 1, the soft metal will start to deform, while the hard metal remains undeformed. Work hardening caused by the plastic deformation of the soft metal, and friction between the contact interfaces, leads to an increased pressure over the length of zone 1. When this is large enough, the pressure will initiate deformation in the hard material. This is where zone 2 begins. By the end of zone 2, an equal deformation of both metals occur, which is when zone 3 starts. By the end of zone 3, the two materials will be bonded. Contrary to bonding of the same material, the soft part will in this case be thinner than the hard part.

3. Experimental procedure

In the following chapter a brief overview of how the experiments were conducted is presented.

3.1. Base materials

The base materials used in the experimental procedures were aluminum alloys of grades AA5183 and AA1050, delivered in the form of spools of ⌀1.6 mm welding wires. Each spool was cut into short lengths of 60 mm. Their butt ends were ground with sandpaper in an attempt to obtain a flat and smooth surface area. Chemical compositions of the two base materials are given in Table 3.1.

Table 3.1: Chemical composition of the alloys used in the experiments.

Alloys	Chemical Composition (wt%)									
	Si	Fe	Cu	Mn	Mg	Cr	Zn	Ti	Be	Al
AA5183[i]	0.05	0.17	0.01	0.63	4.88	0.09	0.01	0.08	0.0002	Balance
AA1050[ii]	0-0.25	0-0.4	0-0.05	0-0.05	0-0.05	N/A	0-0.07	0-0.05	N/A	Balance

[i] According to mill certificate [ii] According to international alloy designations

3.2. Series I: Soft annealing experiments

Previous research [17] has shown that the hardness on the AA5183 alloy being used in these experiments is very high. This is probably a result of cold-drawing. In order to determine the response of the work-hardened alloy to annealing, heat treatments at 100°C, 200°C, 300°C and 400°C for 30 minutes were performed. An oil bath was used for the heat treatments up to 200°C, while a salt bath was used at 300°C and above.

3.2.1. Light microscopy

One sample from each heat treatment, along with one non-treated sample, were cut into smaller pieces and separately embedded in an epoxy mixture of ClaroCit Liquid and ClaroCit Solid. The samples were then ground with sandpaper to a finishing in the range from 320 to 4000 mesh on a Struers Knuth-Rotor. Afterwards, the samples were polished on a Struers DP-U3 unit with polishing discs from 6 µm to 1 µm. The polished samples were then anodized. The purpose of the anodizing was to reveal the microstructure in the sample with the help of λ-plates and polarized light. When the previously mentioned steps were completed, the samples were analyzed in a metallurgical Axiovert 25 light microscope and pictures were taken of the microstructure at different magnifications. Each sample was cleaned with water and ethanol before and after each preparation step.

3.2.2. Hardness measurements

After the microstructure analysis, each sample was subjected to hardness measurements in a Matsuzawa Seiki DVK-1S hardness tester. A load of 1 kg was applied and a total of five measurements were taken for each sample with a 1 mm distance in-between each measurement. Figure 3.1 shows a schematic representation of how the hardness measurements were performed.

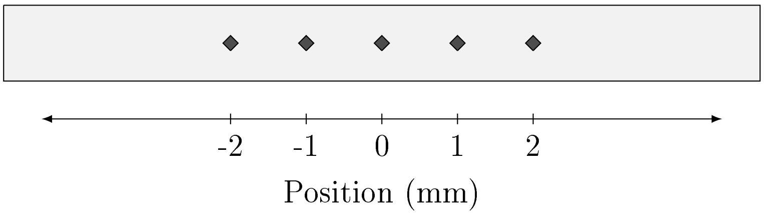

Figure 3.1: Sketch showing how the hardness measurements were performed in Series I.

3.3. Series II & III: Cold pressure welding experiments

3.3.1. Welding equipment

The manually operated CPW machine shown in Figure 3.2 was used in the welding experiments. This type of welding machine is used to weld together electrical copper wires in the field. It works by placing the two wires to be welded on top of the machine, facing each other's short end. This can be seen in Figure 3.2(b). By pulling the handle, the jaws will grab both wires and force them together. Repeated upsetting will increase the amount of compression and plastic deformation.

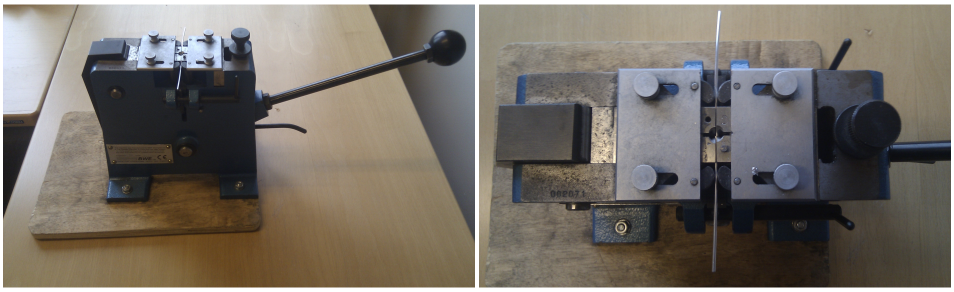

(a) (b)

Figure 3.2: Photograph of the manually operated CPW machine used in the experiments; (a) side view, (b) top view.

3.3.2. Welding experiments

About 60 samples were used in each experiment, 30 for each alloy combination. The different alloy combinations used are listed in Table 3.2.

Table 3.2: A list of the different alloy combinations used in the experiments.

Series	Alloy 1	Alloy 2
II	AA5183(CD)[i]	AA5183(SA)[ii]
III	AA5183(CD)	AA1050(CD)

[i] CD: Cold-deformed [ii] SA: Soft-annealed

Two-and-two wires were placed in the cold pressure welding machine and different amounts of upsetting was applied. This was done to achieve a correlation between the amount of upsetting applied, or compression performed, and the probability of bonding. The degree of upsetting was evaluated from the change in the total wire length, which was measured with a digital caliper. How the measurements were done is shown in Figure 3.3.

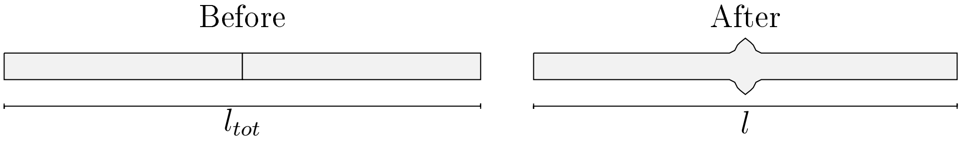

Figure 3.3: Sketches showing how the lengths before and after welding were measured.

Based on the measured wire lengths l_{tot} and l before and after upsetting, the total wire shortening Δl can be calculated from the relationship:

$$\Delta l = l_{tot} - l \tag{3.1}$$

Simple bend testing was then used to determine the resulting bond strength, which involved bending the welded sample three times as shown in Figure 3.4. If the samples did pass this test, by not breaking, the bond was defined as sound. If they failed the outcome was classified as "no bonding". Samples withdrawn in a broken condition from the welding machine were also classified as a "no bonding" case. Figure 3.5 shows examples of the two outcomes from the simple bend testing, i.e. bonding and no bonding.

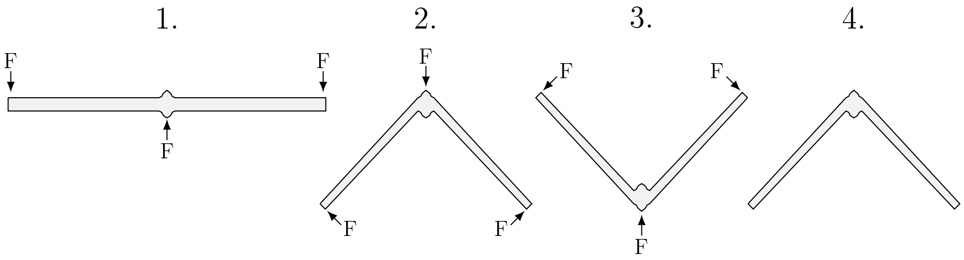

Figure 3.4: Sketches showing the different stages of the bend test.

Note that some of the non-bonded samples were only weakly bonded after welding and therefore broke during the subsequent bend test. These were put aside for further analysis and were marked as "kissing bonds". In addition, a few samples of each combination were welded purely for microstructure analysis and hardness measurements. A bend test was not carried out on these samples, as this could affect the later results.

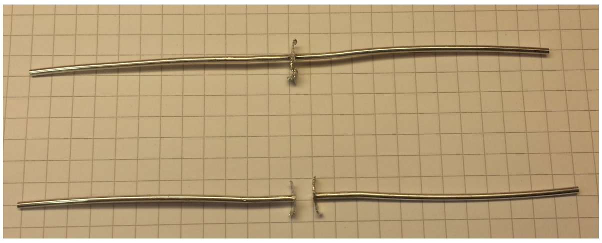

Figure 3.5: Photograph showing examples of successful bonding (top) and a non-successful bonding (bottom).

3.3.3. Light and scanning electron microscopy

The un-bended samples mentioned in Section 3.3.2 were cut short so that the weld zone and roughly 5 mm of each side of the weld were retained. After the cutting, each pair was separately embedded in EpoFix and then subjected to the same preparation procedure as the samples used in soft annealing experiments (see Section 3.2.1). Briefly summarized, the procedure involved grinding down to a surface finish of 4000 mesh followed by polishing down to 1 µm. Once fully polished, one sample from each combination was first anodized and then analyzed in a metallurgical Axiovert 25 light microscope, where pictures were taken at different magnifications. The samples labeled as "kissing bonds" in Section 3.3.2 were subjected to SEM analysis in a Zeiss Supra 55VP scanning electron microscope. The contact sections were closely examined at different magnifications to evaluate the fracture surface appearance.

3.3.4. Hardness measurements

After the completion of the light microscopy analysis, the samples were subjected to hardness measurements in a Matsuzawa Seiki DVK-1S hardness tester. A load of 1 kg was applied and a distance of 0.5 mm between each measurement was performed, as shown in Figure 3.6. In order to make sure that one imprint did not affect the other one, a minimum spacing of at least six times the imprint size was used. The applied interspacing of 0.5 mm is well above this minimum distance. A total of 13 hardness measurements were done on each sample, resulting in a total of 130 individual imprints per specimen.

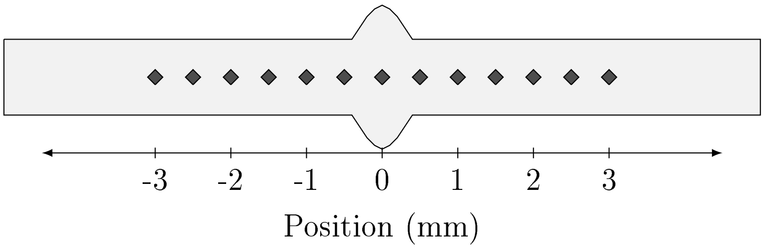

Figure 3.6: Sketch showing how the hardness was measured on the cold-welded samples (Series II and III).

3.3.5. Additional testing of samples from Series III

In addition to the previously mentioned tests, a set of microhardness measurements at a load of 5g as well as a Differential Interference Contrast (DIC) analysis were conducted on samples from Series III. This was done in order to more accurately depict the hardness distribution of the weld zone and to disclose the origin of a dark demarcation line being observed along the joint line in the optical microscope.

4. Results

In the following chapter the results obtained in the CPW experiments will be presented and briefly explained. Note that the optical microscope pictures shown of the cold-welded samples are viewed in the length direction of the joint with the joining zone centered in the middle.

4.1. Series I: Soft-annealing experiments

4.1.1. Microstructure of cold-deformed and soft-annealed samples

Figure 4.1 shows examples of the microstructure before and after soft-annealing. In the as-deformed condition the grains are heavily deformed and strongly elongated in the wire length direction, as shown in Figure 4.1(a). This is typical of cold-drawn wires.

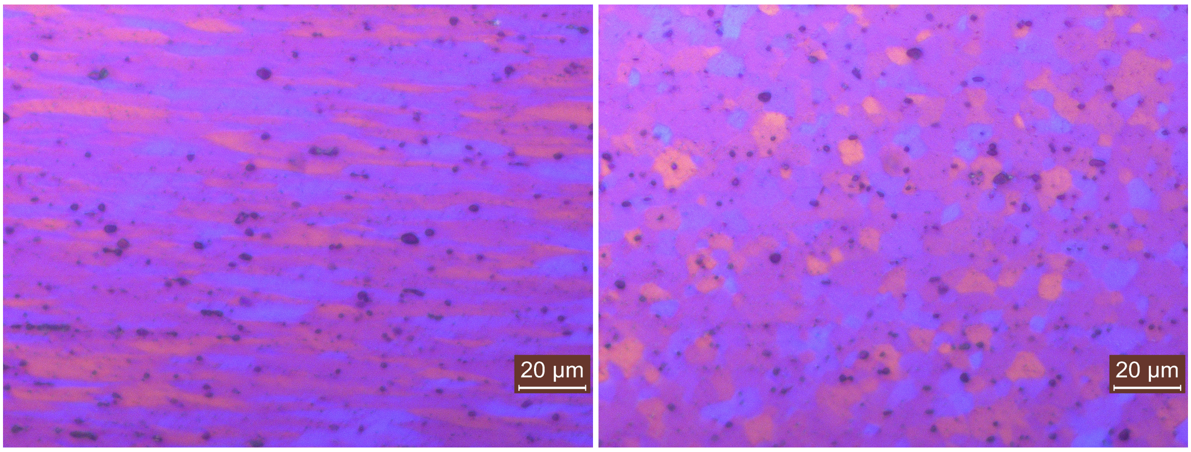

(a) (b)

Figure 4.1: Optical microscope picture of the microstructure of AA5183 (a) before and (b) after heat treatment at 400°C.

After heat treatment at 400°C (Figure 4.1(b)) the AA5183 alloy has fully recrystallized forming new equiaxed grains. The driving force for this reaction is the reduction in the overall dislocation density of the alloy, which facilitates the nucleation and growth of new "deformation-free" grains at the expense of the old deformed ones.

Appendix A contains a collection of micrographs covering the whole temperature range. These micrographs show the progress of the recrystallization process in the AA5183 alloy during soft-annealing.

4.1.2. Hardness reduction during soft-annealing

Figure 4.2 shows the measured hardness after heat treatment at each temperature. It follows that the hardness drops significantly within the temperature range from 100°C to 300°C. Before the recrystallization process starts the hardness reduction is caused by recovery, while the remaining hardness drop at temperatures above, say, 200°C is due to recrystallization. Full soft-annealing is obtained at temperature above about 300°C.

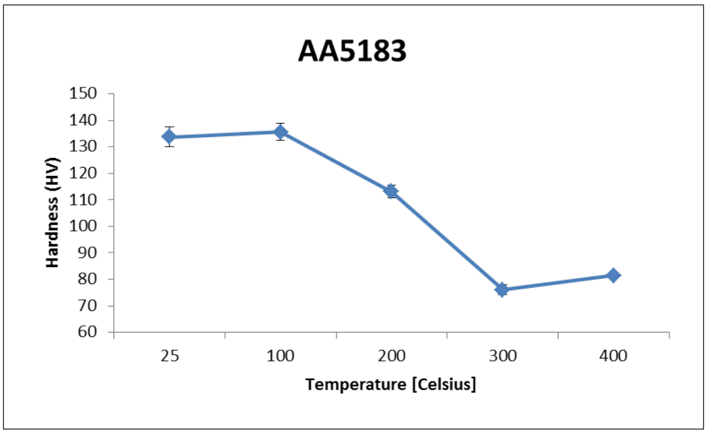

Figure 4.2: Graphical representation of the measured hardness drop in the cold-deformed AA5183 alloy following soft-annealing at different temperatures. The error bars in the graph represent standard deviation of the hardness measurements.

Note that the small hardness increase observed at 400°C in Figure 4.2 is believed to be caused by natural ageing following prolonged room temperature storage of the sample.

4.2. Series II & III: Cold pressure welding experiments

4.2.1. Microstructure and flow pattern within the weld zone

Figure 4.3 below shows an optical micrograph of the weld zone following joining of cold-deformed AA5183 (top half) to soft-annealed[1] AA5183 (bottom half). Although the microstructure of the top and bottom parts of the joint are not clearly revealed in this specific picture, the base material microstructures correspond to those shown in Figure 4.1. The flow lines start to bend outwards when entering the deformation zone, thereby pushing oxide-containing material out from the weld zone and into the flash constituting the surrounding collar. This flash can be seen on either side in the middle of the picture. Regarding the weld zone itself, this seems to be a perfect seam with no cracks or oxide present at the interface.

---

[1] In the present context soft-annealing means heat treatment at 400°C for 30 min prior to joining, in agreement with the hardness data presented previously in Figure 4.2.

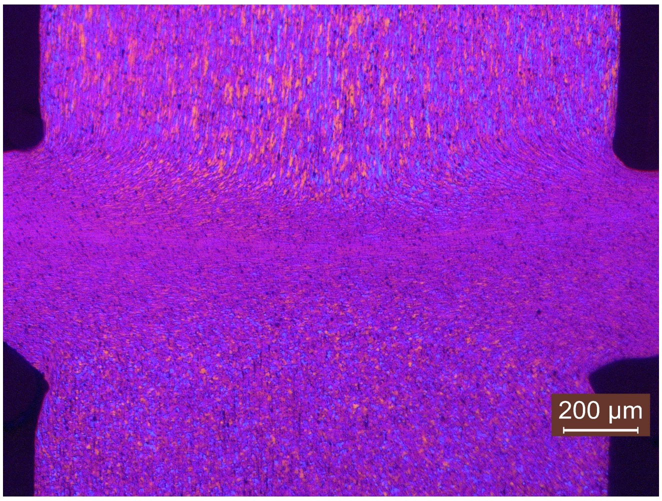

Figure 4.3: Optical microscope collage of the anodized weld zone showing the microstructure and flow pattern within the cold-deformed AA5183 (top) and the soft-annealed AA5183 (bottom) materials.

The third series, involving joining of cold-deformed AA5183 to commercial purity AA1050, gave a different result. As seen from Figure 4.4, the appearance of the weld zone is different compared to the one shown in Figure 4.3. The main difference is the curved contact zone, where the cold-deformed AA5183 (top) is seen to penetrate the softer AA1050 (bottom). A dark demarcation line across the entire weld zone can also be observed. Apart from this, both the material flow pattern and the flash formation are similar.

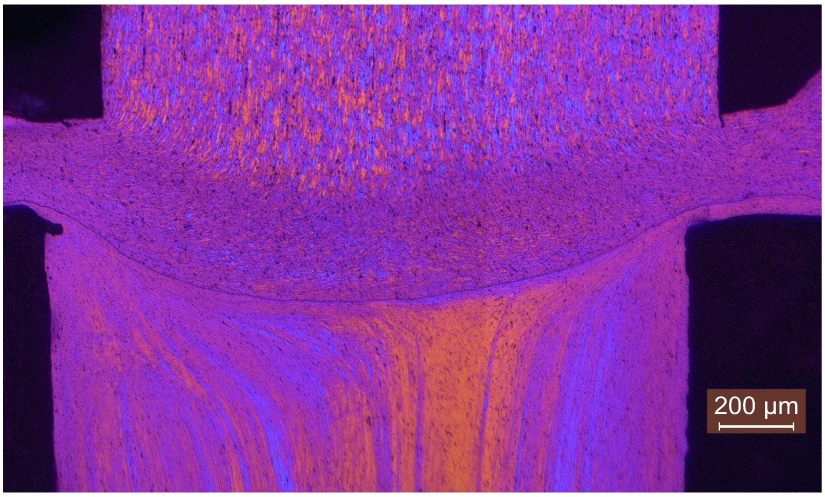

Figure 4.4: Optical microscope collage of the anodized weld zone showing the microstructure and flow pattern within the cold-deformed AA5183 (top) and the commercial purity AA1050 (bottom) materials.

In order to determine whether the dark demarcation line is also visible in normal light, the polarized light was turned off and new pictures taken, as seen in Figure 4.5. Still, the line is present, which calls for further investigations of the origin of this phenomenon (to be disclosed in Section 5.4).

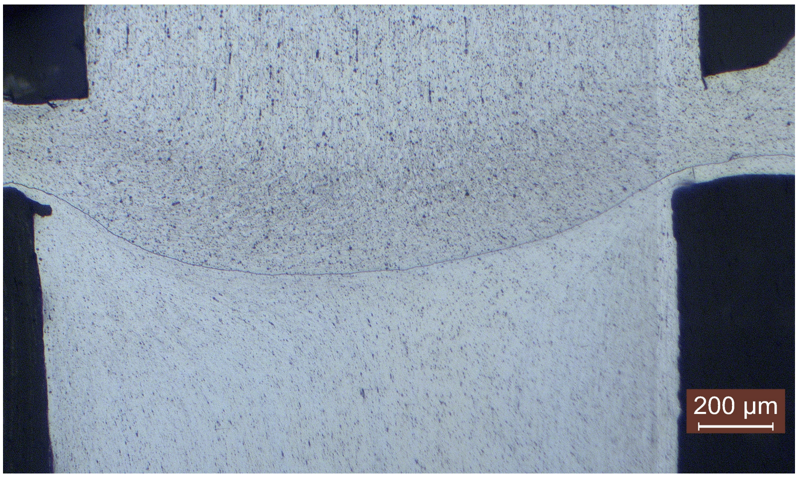

Figure 4.5: Optical microscope collage of the anodized weld zone showing the microstructure and flow pattern within the cold-deformed AA5183 (top) and commercial purity AA1050 (bottom) materials in the absence of polarized light.

4.2.2. Hardness distribution across the weld zones

Figure 4.6 shows the average hardness values across the weld zones in (a) Series II and (b) Series III along with the measured standard deviations. As expected, the measured hardness profiles are seen to be very different between the two series. In Series II the hardness in the soft-annealed AA5183 material increases rapidly with the weld zone, approaching that of the cold-deformed alloy at the contact section. At the same time, a small hardness increase can be observed within the cold-deformed AA5183 material adjacent to the contact section. This type of response is a reflection of the work hardening behavior of Al-Mg alloys - a topic that will be further elaborated and discussed in the next chapter.

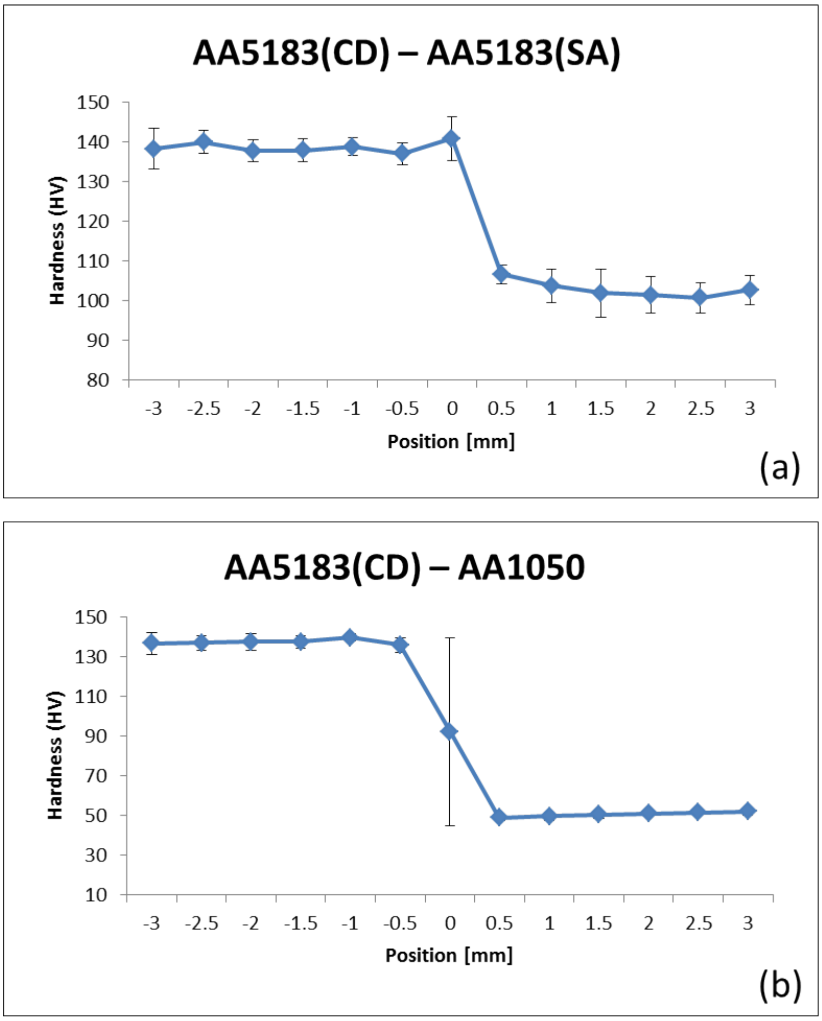

Figure 4.6: Graphical representation of the measured hardness distribution across the weld zone for (a) cold-deformed AA5183 and soft-annealed AA5183 (Series II) and (b) cold-deformed AA5183 and commercial purity AA1050 (Series III). Note the difference in the hardness scale between Series II and III. The error bars in the graphs represent the standard deviation of the hardness measurements.

In contrast, Series III does not reveal evidence of initial work hardening outside the weld zone. Within the weld zone, however, the hardness increases steadily from about 45 Vickers in the commercial purity AA1050 material to approximately 140 Vickers on the other side of the contact section. The latter value is the same as the hardness in the cold-deformed AA5183 material.

Because the size of the hardness impression at a load of 1 kg is much larger than the width of the deformation zone in Series III, Figure 4.6(b) does not reveal the correct hardness distribution within this zone. In the next chapter a more accurate depiction will be presented, based on high-resolution microhardness measurements.

4.3. Bond strength of cold pressure welds

In Figure 4.7 the raw data from the bend testing of the joints produced are presented graphically. In these plots the measured change of length Δl has been converted into nominal strain e_n via Equation 4.1, taking the gauge length l_0 equal to 4 mm (i.e. 2.5 times the diameter of the wire):

$$e_n = \frac{\Delta l}{l_0} = \frac{\Delta l(mm)}{4mm} \tag{4.1}$$

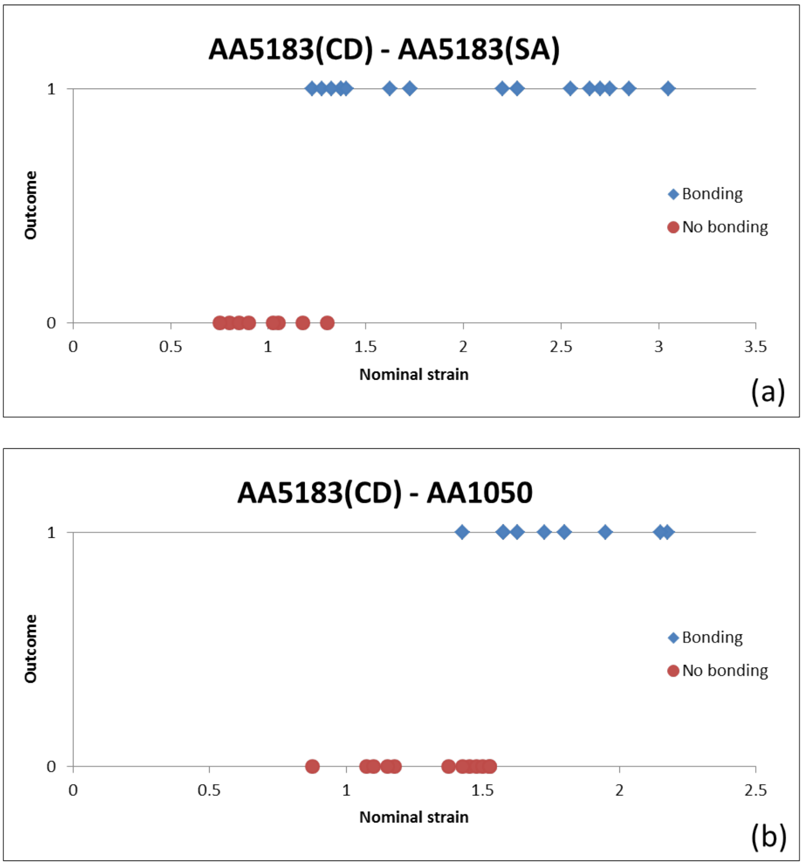

Figure 4.7: Graphical representations of the bend test results obtained in (a) Series II and (b) Series III. In these graphs the final outcome of the bend testing (i.e. bonding or no bonding) is plotted versus the nominal strain e_n, as calculated from Equation 4.1. A value of 1 means bonding, whereas a value of 0 means no bonding.

It can be observed from Figure 4.7 that a nominal strain of about 1.2 is required to initiate bonding in Series II. Still, full bonding cannot be guaranteed before the strain is increased to a value of 1.3. In Series III these threshold values for the nominal strain are raised to 1.4 and 1.5, respectively. But besides that, the two series (i.e. alloy combinations) appear to behave similar in the sense that the transition from no bonding to full bonding takes place within a very small strain interval as soon as the lower threshold strain for bond initiation is reached.

4.4. Fracture surface appearance of broken bend test specimens

Figure 4.8 shows SEM fractographs of broken specimens that did not pass the bend test. These fractographs are therefore representative of the bonding situation existing within the transition region between the no bonding and the full bonding cases in Figure 4.7. Two distinct fracture types can be identified. One corresponds to the smooth areas that tend to dominate the fracture surfaces in Figure 4.8. This type of fracture mode is typical for a "kissing" bond, which refers back to a situation where metallic bonding is prevented locally due to the presence of surface contaminants at the contact section [15, 19]. In-between, evidenced dimples formation can be found. This dimple formation means that full metallic bonding is achieved in other areas along the contact sections, where the local conditions are more favorable and thus contribute to bond initiation at an earlier stage during upsetting.

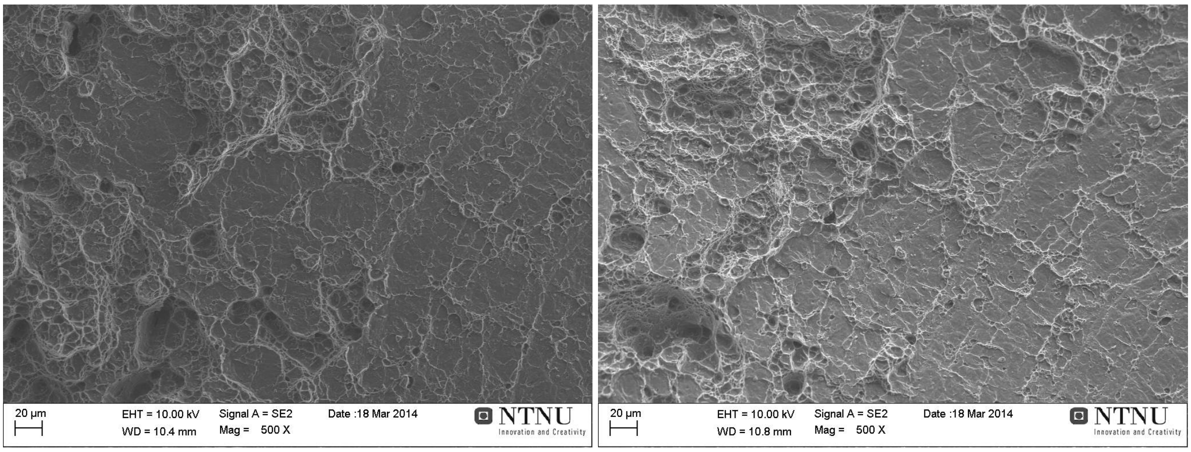
20 µm
EHT = 10.00 kV
WD = 10.4 mm
Signal A = SE2
Mag = 500 X
Date :18 Mar 2014
NTNU
Innovation and Creativity
20 µm
EHT = 10.00 kV
WD = 10.8 mm
Signal A = SE2
Mag = 500 X
Date :18 Mar 2014
NTNU
Innovation and Creativity

(a) AA5183(CD)

(b) AA5183(SA)

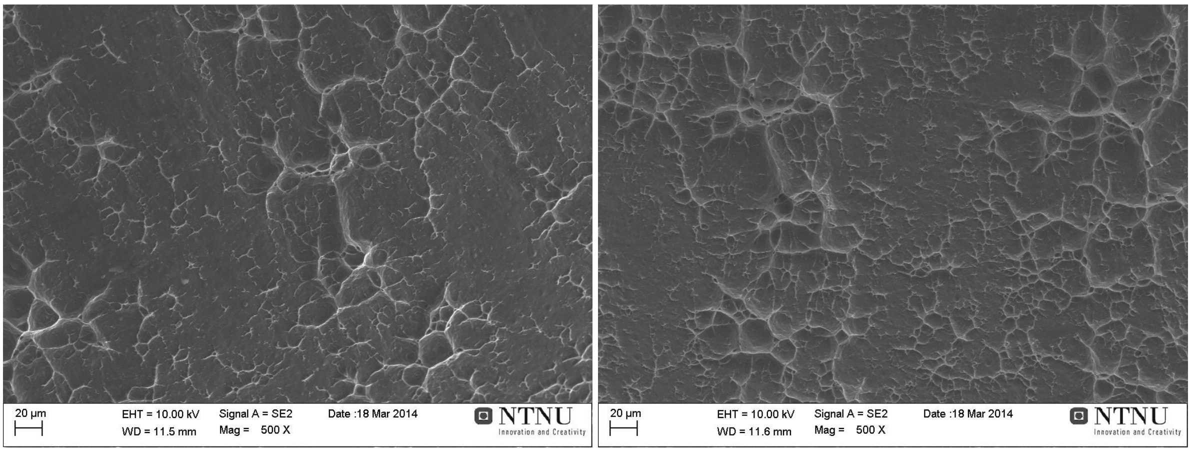
20 µm
EHT = 10.00 kV
WD = 11.5 mm
Signal A = SE2
Mag = 500 X
Date :18 Mar 2014
NTNU
Innovation and Creativity
20 µm
EHT = 10.00 kV
WD = 11.6 mm
Signal A = SE2
Mag = 500 X
Date :18 Mar 2014
NTNU
Innovation and Creativity

(c) AA5183(CD)

(d) AA1050

Figure 4.8: SEM fractographs of broken bend test specimens from (a-b) Series II and (c-d) Series III.

5. Discussion

It is appropriate to start the discussion with a closer look at the material flow pattern and the resulting work hardening behavior contributing to the pressure build-up at the contact surface during CPW of dissimilar aluminum alloys.

5.1. Contact pressure build-up during upsetting

When one of the work-pieces to be joined is softer than the other one, there will be an imbalance in the flow stress of the alloys, as shown schematically in Figure 5.1.

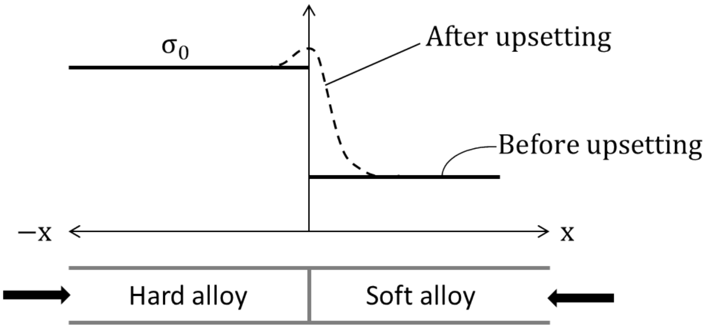

Figure 5.1: Schematic representation of the flow stress σ_0 profiles before and after upsetting during CPW of two dissimilar alloys.

After upsetting has started and the material begins to flow out from the weld zone and into the flash constituting the surrounding collar, the pressure on each side of the contact section must be the same, as indicated by the broken part of the flow-curve in Figure 5.1. In principle, there are two different ways the soft material can adapt to this situation; i.e. either by pure work-hardening as in Series II or through build-up of an internal extrusion pressure by allowing the harder alloy to penetrate the softer one as in Series III.

In Series II the stress-strain curve for AA5083 reproduced in Figure 5.2 can be used to explain the pressure build-up at the contact section when cold-deformed AA5183 is welded to soft-annealed AA5183.

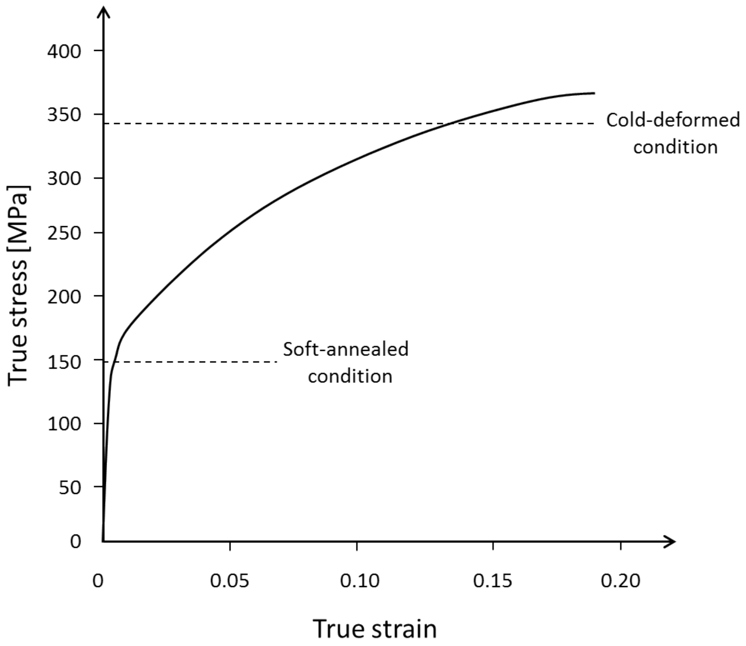

Figure 5.2: Experimental stress-strain curve for AA5083. The re-drawing is based on data from Ref. [20].

It follows from Figure 5.2 that the soft-annealed alloy work-hardens very rapidly and will already at a strain of 0.15 to 0.20 have reached the flow stress of the cold-deformed alloy. At the same time the initial flow stress of the cold-deformed alloy is approaching its saturation value and will thus barely increase during further upsetting.

In Series III the situation is different, as the soft commercial purity AA1050 material work-hardens to a much lesser extent compared to the soft-annealed AA5183, as shown in Figure 5.3. Therefore, there will be a large mismatch between the flow stress of the cold-deformed AA5183 material and the commercial purity AA1050 material after the initial compression of the specimens has occurred. This, in turn, facilitates penetration of the former one into the latter one. Then the pressure at the contact section starts to build up, and will eventually reach the flow stress of the cold-deformed AA5183 alloy. At this stage the mating of the two surfaces begins and bonding is initiated.

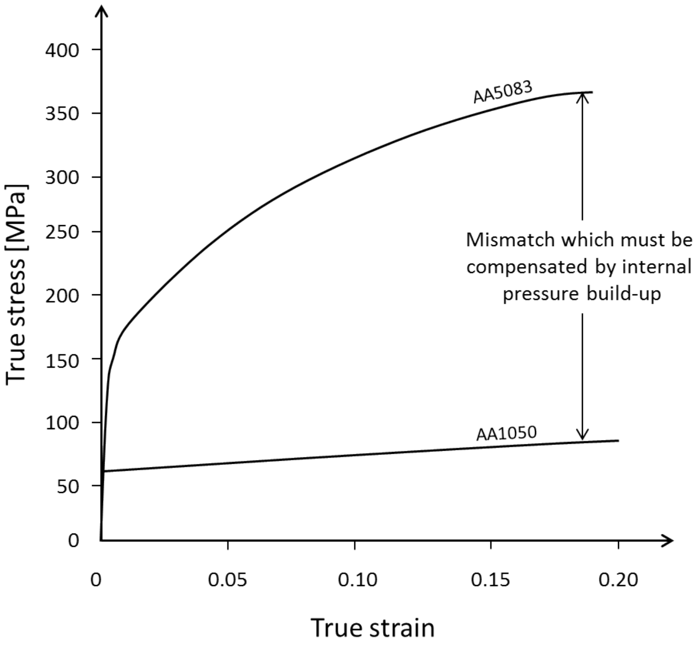

Figure 5.3: Experimental stress-strain curves for AA5083 and AA1050 superimposed in the same diagram. The re-drawing is based on data from Refs. [14, 20].

5.2. Steepness of hardness gradient across the weld zone

To further investigate the weld zone of Series III, micro-hardness measurements were performed on each side of the contact surface at three different locations (see Figure 5.4). In this case a load of 5g is used, which creates impressions that are sufficiently small to sample the local areas in the vicinity of the contact section as well.

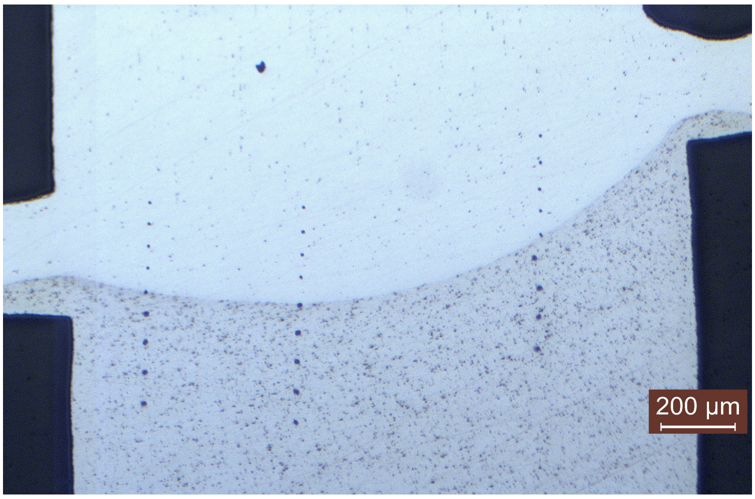

Figure 5.4: Optical microscope collage showing the micro-hardness imprints taken across the weld zone of cold deformed AA5183 (top) and commercial purity AA1050 (bottom).

The corresponding measured hardness values are presented graphically in Figure 5.5. Figure 5.5(a) provides the individual hardness profiles for all three locations, while Figure 5.5(b) shows the average one. From these graphs it is evident that the hardness gradient across the weld zone is actually much steeper than that inferred from the data in Figure 4.6(b). As a matter of fact, it can just barely be resolved using micro-hardness measurements. At first glance, the observation is surprising, considering the fact that pressure at the contact surface must be equal to the flow stress of the cold-deformed AA5183 material before mating starts and bonding is initiated. But the explanation is simple, as the soft AA1050 material cannot match its counterpart's flow stress through ordinary work-hardening (see Figure 5.3). Instead, the hard AA5183 wire acts as a piston by penetrating the soft one, as shown previously in Figure 4.4, which leads to build-up of an internal extrusion pressure in the vicinity of the contact surface. When the specimen then is removed from the clamps, this extrusion pressure (which is hydrostatic in nature) is released and all traces of it becomes immediately wiped out.

It is also worth noting that the three different hardness values referring to the interface position 0 in Figure 5.5(a) can be visually explained by examining the imprints in Figure 5.4. By taking a closer look at the contact surface imprints it is obvious that only the leftmost imprint hits spot-on. The middle and rightmost ones hit slightly below and above the contact section, respectively. Although their locations are off by just a few µm, the measured hardness values are highly different. This, once again, suggests that the hardness gradient is incredibly steep.

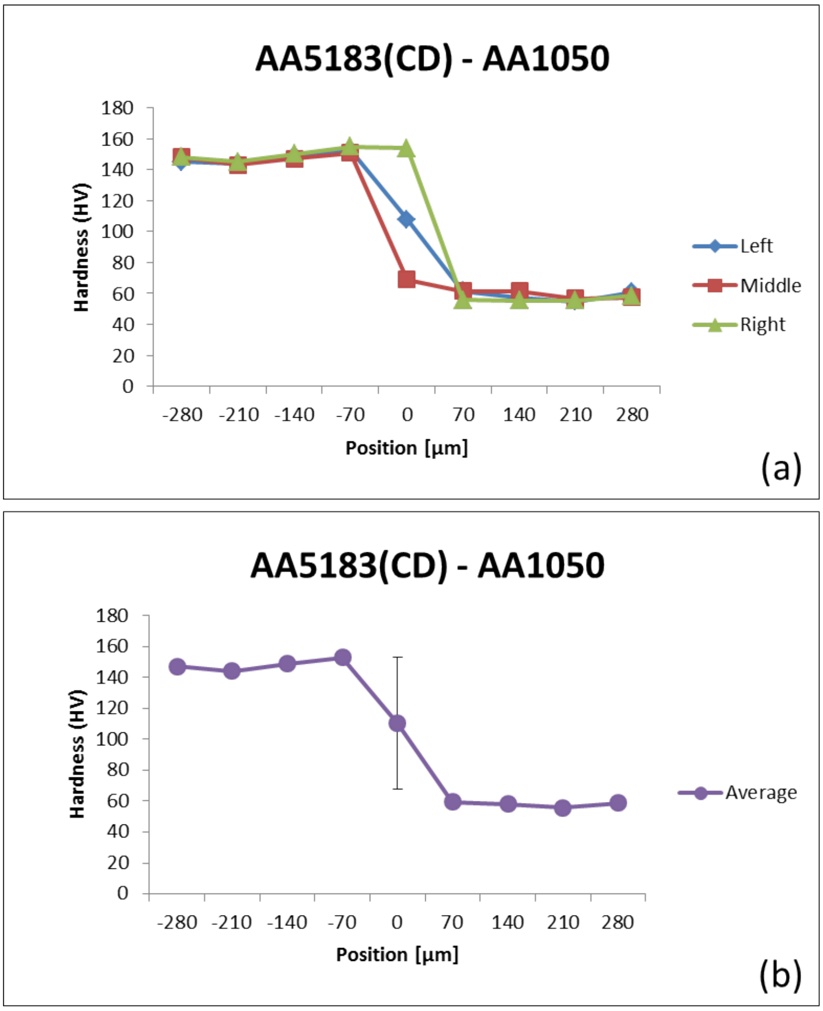

Figure 5.5: Results from micro-hardness measurements carried out across the weld zone of cold-deformed AA5183 and commercial purity AA1050; (a) individual hardness profiles for all three locations indicated in Figure 5.4, (b) average hardness profile across the weld zone. The error bar in the lower graph represents the standard deviation of the hardness measurements.

Figure 5.6 is constructed by combining data from Figure 5.5(b) with data from Figure 4.6(b). The resulting plot shows the micro-hardness measurements in conjunction with the macro-hardness measurements. In areas located closer than 500 µm from the center (corresponding to the weld zone) the hardness increases. This indicates that both alloys do work-harden to a certain extent before the steep extrusion pressure gradient is established at the contact surface.

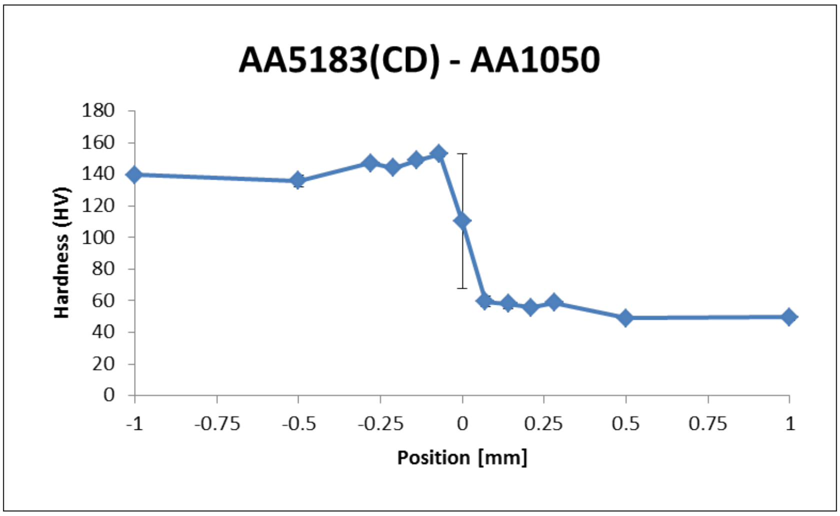

Figure 5.6: Graphical representation of the combined macro- and micro-hardness data for cold-deformed AA5183 and commercial purity AA1050. The error bar in the graph represents the standard deviation of the hardness measurements.

5.3. Material flow pattern during upsetting

When two dissimilar aluminum alloys are joined together by means of CPW, one would intuitively expect that the softest alloy becomes more plastically deformed compared with the hardest one. Therefore, separate measurements of the actual change of length of the softest specimen during upsetting have been carried out for both sets of alloy combinations. The results are presented graphically in Figure 5.7.

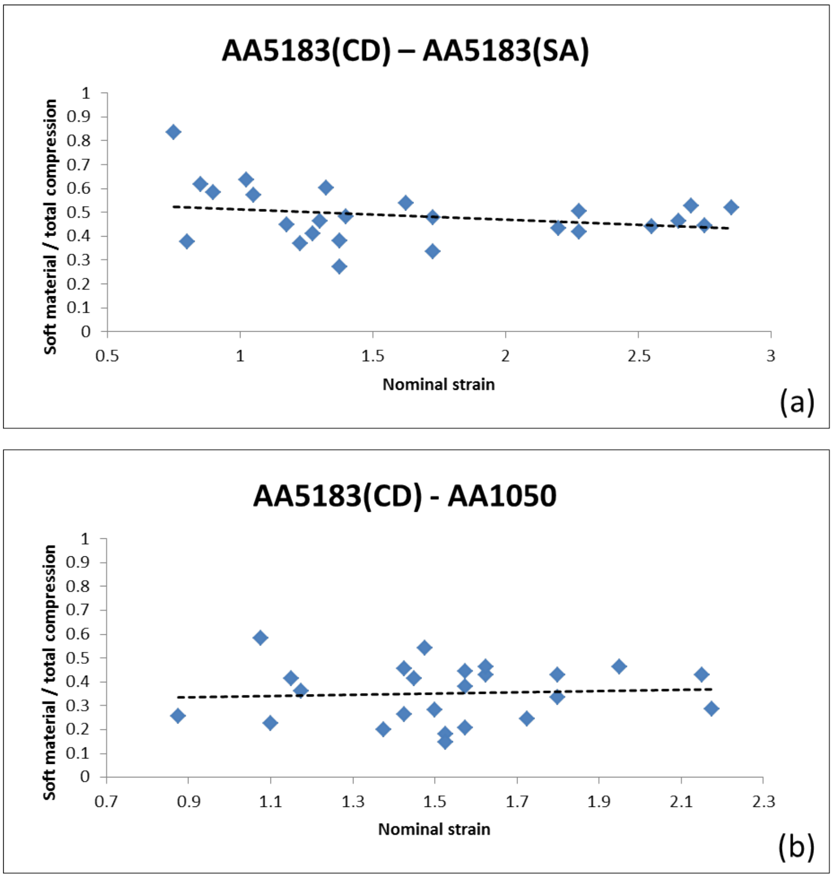

Figure 5.7: Graphical representations of the actual change of length of the softest specimen compared to the total measured change of length during upsetting of (a) cold-deformed AA5183 and soft-annealed AA5183 (Series II) and (b) cold-deformed AA5183 and commercial purity AA1050 (Series III).

It follows from Figure 5.7 that there is no significant change in the deformation behavior of the materials during upsetting. As a matter of fact, the trend-lines suggest that the softest alloys appear to plastically deform less than their hard cold-worked counterparts at virtually all nominal strain values. This is probably a reflection of the confined weld zones being observed previously in Figures 4.3 and 4.4, which allows the flash material to escape through the gap between the clamps holding the specimens in place without contributing to excessive work-hardening (see Figures 4.6 and 5.5).

Referring to Figure 5.8, the material flow pattern during upsetting can now be sketched as follows. In Series II, the bulk material on both sides of the joint line will probably escape through the gap between the clamps as soon as the flow stress of the respective alloys are reached. Most of the observed flash formation is presumably a result of such bulk material flow, as indicated by the magnitude and direction of the arrows in Figure 5.8(a). In contrast, the work-hardened material adjacent to the contact surface is pushed outwards at a much lower velocity (i.e. rate). Hence, both the local surface expansion and the corresponding surface exposure at the interface are probably significantly lower than those calculated from simple measurements of the total change of length of the specimens during upsetting. This, in turn, will influence the bonding conditions during CPW and the interpretation of the experimental results in Figure 4.7.

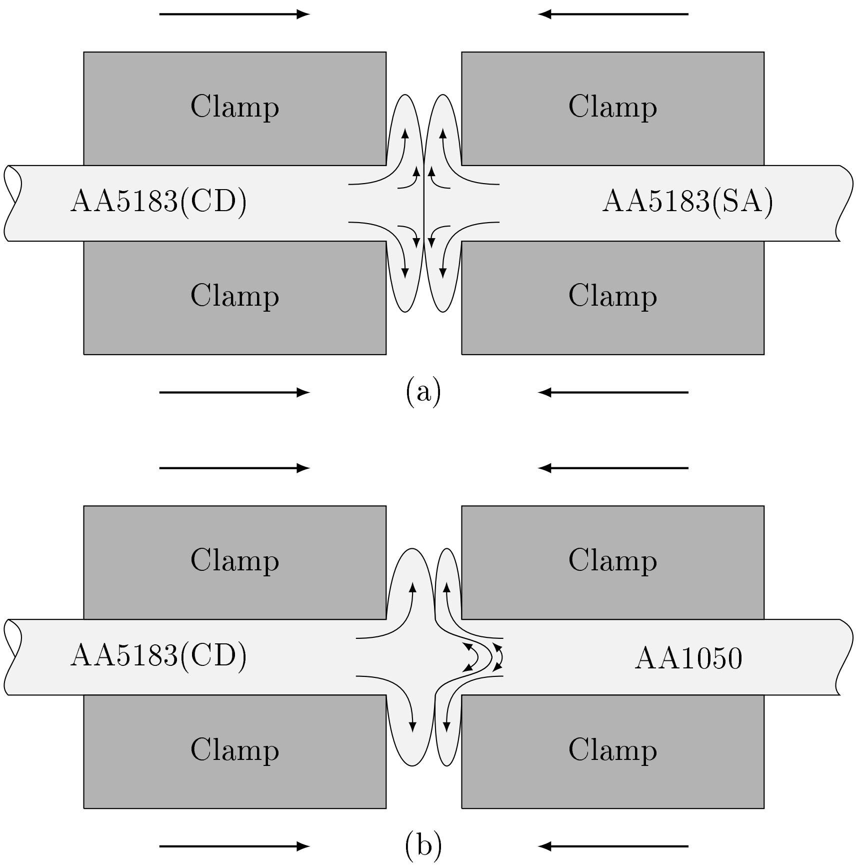

Figure 5.8: Schematic illustrations of the assumed material flow pattern during CPW of (a) cold-deformed AA5183 and soft-annealed AA5183, (b) cold-deformed AA5183 and commercial purity AA1050. The arrows in the sketches indicate the magnitude and direction of the material flow at the different locations.

A similar situation also exists during CPW of cold-deformed AA5183 to commercial purity AA1050, although the material flow pattern in this case is even more complex, as indicated in Figure 5.8(b). But the conveyed message is the same, i.e. that most of the observed plastic deformation occurring during upsetting is a result of flow of the softer bulk materials located on either side of the contact section. At the same time the work-hardened material close to the interface experiences a much smaller deformation and thus a lower surface expansion and surface exposure than the bulk material.

5.4. Origin of dark demarcation line at joint interface

In order to determine whether or not the previously observed dark demarcation line in Figures 4.4 and 4.5 is an artifact or not, a new metallographic sample was prepared. Each step of the process was then documented to disclose the origin of this phenomenon.

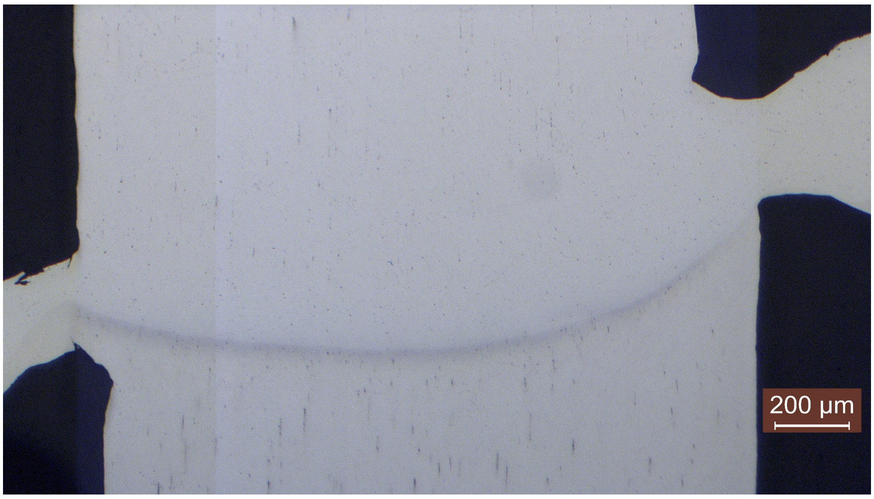

Figure 5.9: Optical microscope collage of the pre-anodized weld zone of cold-deformed AA5183 (top) and commercial purity AA1050 (bottom).

Figure 5.9 shows a polished sample in normal light. There is no longer sign of the dark demarcation line shown previously in Figures 4.4 and 4.5. However, there seems to be a change of level between the two alloys. With the suspicion that this may be the reason for the origin of the phenomenon in mind, the sample was put into a Leica MEF4M microscope for Differential Interference Contrast (DIC) analysis. The resulting micrograph can be seen in Figure 5.10. This micrograph shows a distinct shadow originating from a change of level between the two specimens.

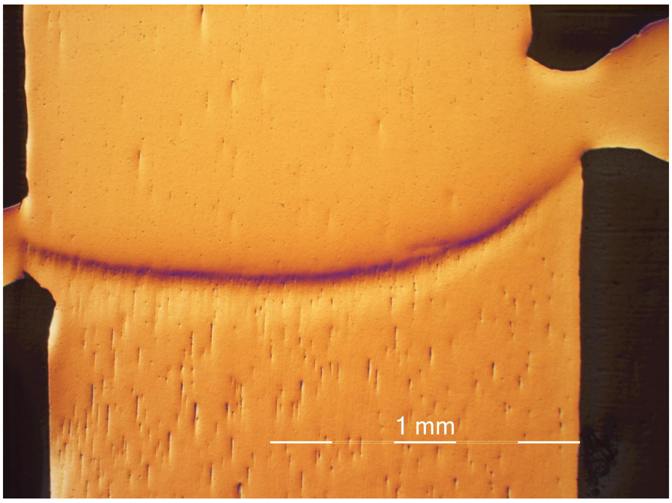

Figure 5.10: Optical microscope picture of the weld zone of cold-deformed AA5183 (top) and commercial purity AA1050 (bottom) as viewed in the DIC mode.

The sample was then anodized to see if this would produce a dark demarcation line. Figures 5.11 and 5.12 show the anodized sample in normal and polarized light, respectively. The dark demarcation line has reappeared, indicating that the anodizing process is the source.

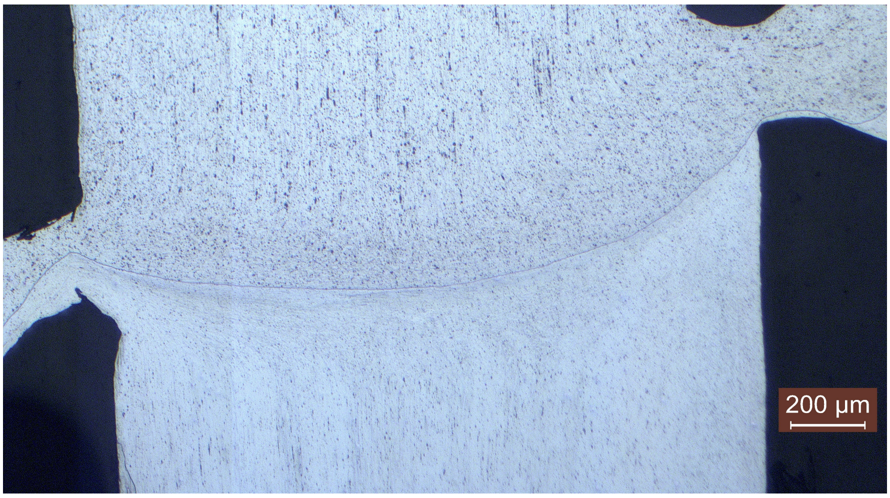

Figure 5.11: Optical microscope collage of the anodized weld zone of cold-deformed AA5183 (top) and commercial purity AA1050 (bottom) as viewed in normal light.

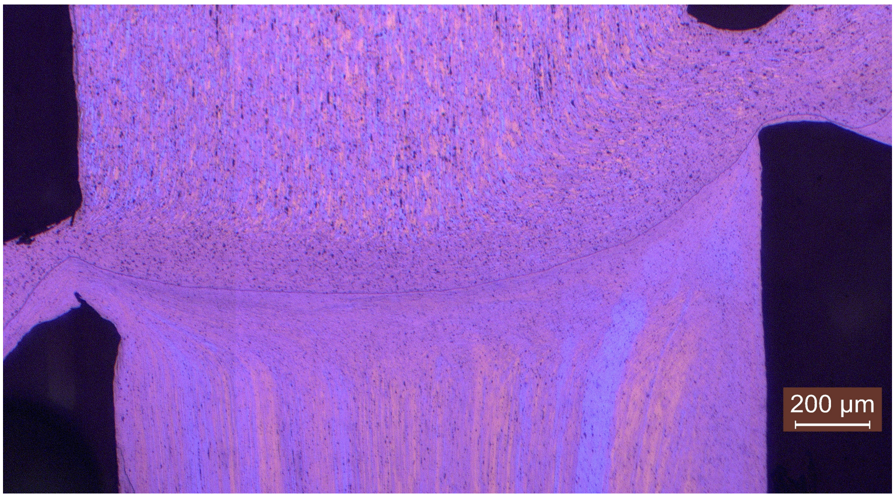

Figure 5.12: Optical microscope collage of the anodized weld zone of cold deformed AA5183 (top) and commercial purity AA1050 (bottom) as viewed in polarized light.

In order to fully disclose the origin of the dark demarcation line, a new DIC analysis was performed on the anodized sample. The result is shown in Figure 5.13. Once again a shadow is observed, with the demarcation line located in the middle. This strongly suggests that the line is simply the edge of the cliff being established during simultaneous grinding and polishing of the two samples with highly different mechanical properties (i.e. hardness values).

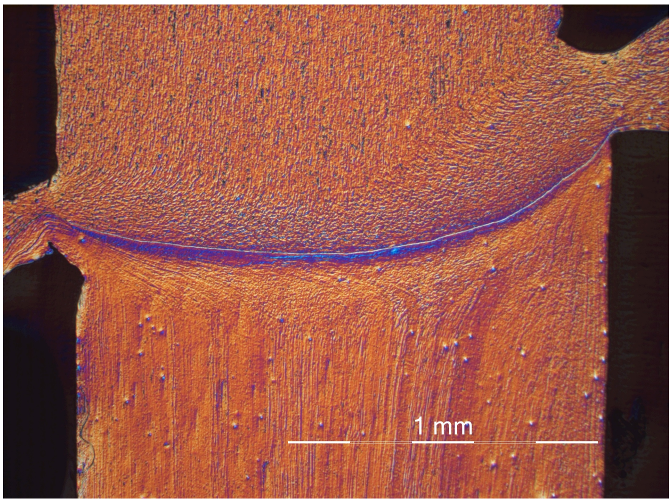

Figure 5.13: Optical microscope picture of the anodized weld zone of cold-deformed AA5183 (top) and commercial purity AA1050 (bottom) as viewed in the DIC mode.

5.5. Statistical analysis of the bend test results

A statistical analysis of the bend test results can be performed by converting the data from Section 4.3 into a corresponding probability of bonding $P(B)$ via the equation:

$$P(B) = \frac{\#\, of\, bonded\, samples}{Total\ \#\ of\ samples} \tag{5.1}$$

By sub-dividing the nominal strain e_n into smaller strain intervals it is possible to calculate the gradual change in $P(B)$ from 0 to 1. In this analysis a fixed strain interval of 0.10 is used within the narrow range where there are two outcomes, i.e. bonding or no bonding. The calculated values for $P(B)$ are summarized in Tables 5.1 and 5.2 for Series II and III, respectively.

Table 5.1: Calculated values for the probability of bonding during CPW of cold-deformed AA5183 and soft-annealed AA5183 within different strain intervals (Series II).

Nominal strain e_n	# of bonded samples	# of unbonded samples	Total # of samples	Probability of bonding $P(B)$
< 1.20	0	7	7	0
1.20 - 1.30	2	1	3	0.67
> 1.30	16	0	16	1

Table 5.2: Calculated values for the probability of bonding during CPW of cold-deformed AA5183 and commercial purity AA1050 within different strain intervals (Series III).

Nominal strain e_n	# of bonded samples	# of unbonded samples	Total # of samples	Probability of bonding $P(B)$
< 1.40	0	8	8	0
1.40 - 1.50	1	4	5	0.20
1.51 - 1.60	3	2	5	0.60
> 1.60	6	0	6	1

5.5.1. Cumulative probability for bonding

Figure 5.14 shows the cumulative probability of bonding as a function of nominal strain based on the values from Tables 5.1 and 5.2. As expected, the probability of bonding is seen to increase very rapidly from 0 to 1 within a very narrow strain interval for both sets of alloy combinations - slightly more so in Series II than in Series III.

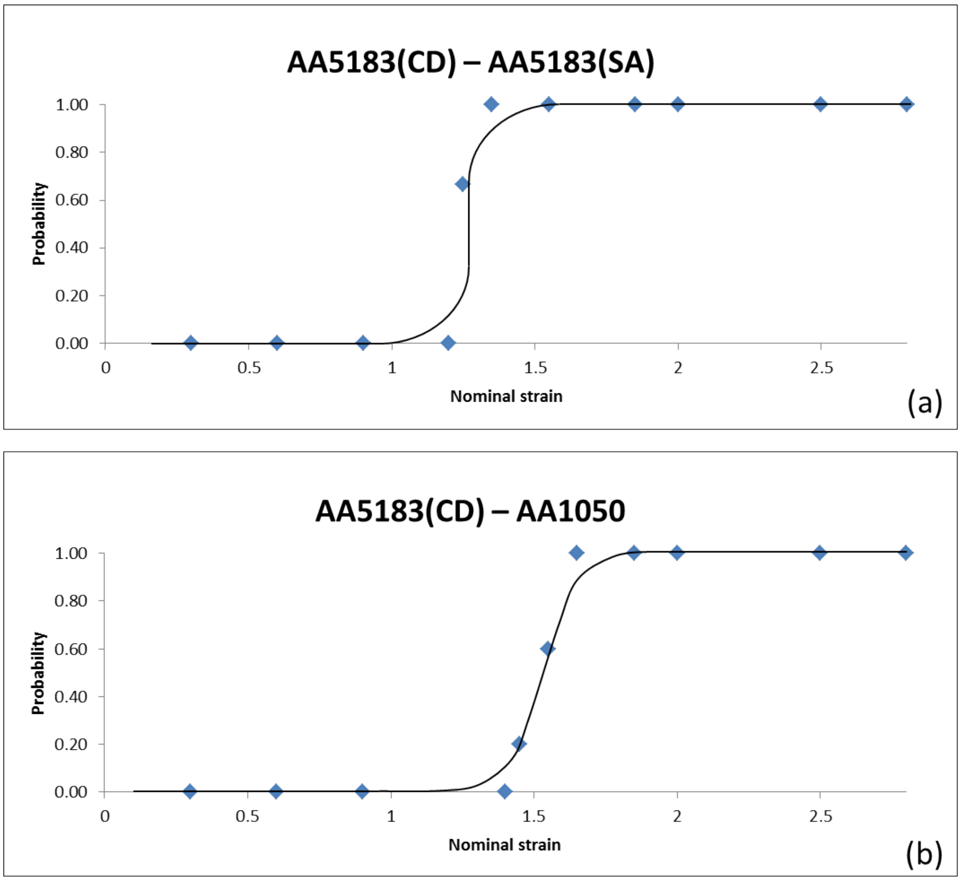

Figure 5.14: Plots showing the cumulative probability of bonding as a function of nominal strain for (a) Series II and (b) Series III.

By calculating the mean and standard deviation of the mean from the probability curves in Figure 5.14 it is possible to calculate the nominal strain required to obtain bonding at different levels of probability, as shown in Table 5.3.

Table 5.3: Nominal strain required to achieve bonding in Series II and III at different levels of probability.

Alloys (strain)	P(X $\leq$ x) =					
	0.999	0.995	0.950	0.900	0.800	0.050
Series II (e_n)	1.42	1.40	1.35	1.33	1.31	1.19
Series III (e_n)	1.87	1.81	1.71	1.67	1.62	1.35

By choosing $P(X \leq x) = 0.05$ as the lower limit for bond initiation and $P(X \leq x) = 0.995$ as the corresponding limit for full bonding it is now possible to compare the two series. It follows that metallic bond initiation occurs generally at a lower nominal strain in Series II than in Series III. The same is also true for full bonding.

5.5.2. Surface expansion and surface exposure of the bulk materials

Another way of presenting the difference in the bonding characteristics between Series II and III is through calculation of the surface expansion and surface exposure, as defined previously in Section 2.1.3. The dashed line in Figure 5.15 indicates the section of which these values refer back to.

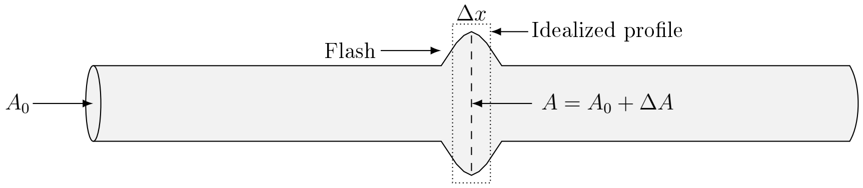

Figure 5.15: Sketch showing how the surface expansion and the surface exposure can be calculated from measurements of the flash thickness Δx.

The calculated values for the surface expansion and surface exposure are listed in Table 5.4, using Equations 2.1 and 2.2.

Table 5.4: Calculated values for the surface expansion and surface exposure needed to achieve bond initiation at $P(X \leq x) = 0.05$ (left values) and full bonding $P(X \leq x) = 0.995$ (right values), respectively in Series II and III.

Alloys	Surface expansion, $\frac{A}{A_0}$		Surface exposure, Y	
Series II	16.87	19.67	0.94	0.95
Series III	19.00	25.13	0.95	0.96

It can be seen from Table 5.4 that full bonding requires a surface exposure of above 0.95-0.96 both in Series II and III. These results are consistent with those reported by others for CPW of aluminum alloys [14–17, 21].

5.6. Cold bonding mechanism in dissimilar aluminum joints

The results presented previously in Figure 5.14 show that the transition from no bonding to full bonding takes place within a small strain interval as soon as the critical upsetting for metallic bond initiation is reached. In the following, a plausible explanation to these previous experimental observations will be presented, based on an analysis of the local deformation occurring at the contact section during upsetting.

Figure 5.16 shows a schematic drawing of the contact section, as viewed normal to the wire length direction.

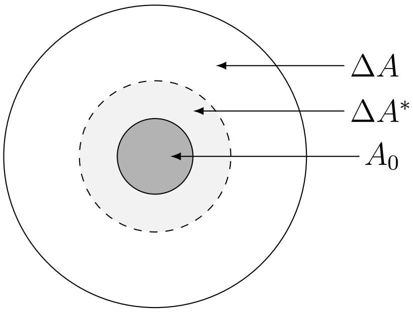

Figure 5.16: Schematic drawing of the contact section, as viewed normal to the wire length direction. In this case A_0 is the nominal wire cross section, while ΔA^* is the new interfacial area and ΔA is the total surface area, respectively, which form during upsetting.

Let z now define the ratio between ΔA^* and ΔA, i.e.

$$z = \frac{\Delta A^*}{\Delta A} \tag{5.2}$$

with the restriction $0 \leq z \leq 1$.

Then it follows from Figure 5.15 and Equation 5.2 that:

$$\Delta A = A_0 \frac{\Delta l}{\Delta x} = \frac{\Delta A^*}{z} \tag{5.3}$$

from which

$$\Delta A^* = A_0 \frac{\Delta l}{\Delta x} z \tag{5.4}$$

and

$$A^* = A_0 + \Delta A^* = A_0(1 + \frac{\Delta l}{\Delta x} z) \tag{5.5}$$

where A^* now refers to the total interfacial cross section area.

Based on Equation 2.2, the actual interface surface exposure Y^* can be defined as:

$$Y^* = \frac{A^* - A_0}{A^*} \tag{5.6}$$

which after substitution and some further manipulation reads:

$$Y^* = \frac{e_n \, l_0 \, z}{\Delta x + l_0 \, z} \tag{5.7}$$

Substituting $l_0 = 4$ mm and $\Delta x = 0.3$ mm into Equation 5.7 then gives:

$$Y^* = \frac{4 \, e_n \, z}{0.3 + 4 \, e_n \, z} \tag{5.8}$$

Figure 5.17 shows a graphical representation of Equation 5.8, in which Y^* is plotted versus e_n for different z-values. It follows that a possible constrained deformation of the interface compared to the bulk material due to differences in the flow behavior means that metallic bonding in a real joining situation occurs at a much lower surface exposure than that inferred from Figure 5.14. For example, at a nominal strain $e_n = 1$ the calculated surface exposure for the bulk material ($z = 1$) is about 0.93, whereas the actual interface Y^*-value at the same time may be as low as 0.73. This is an important observation in the sense that it sheds new light upon the bonding mechanism in CPW in general and dissimilar aluminum joint in particular that have not previously been reported by others [14–17, 21].

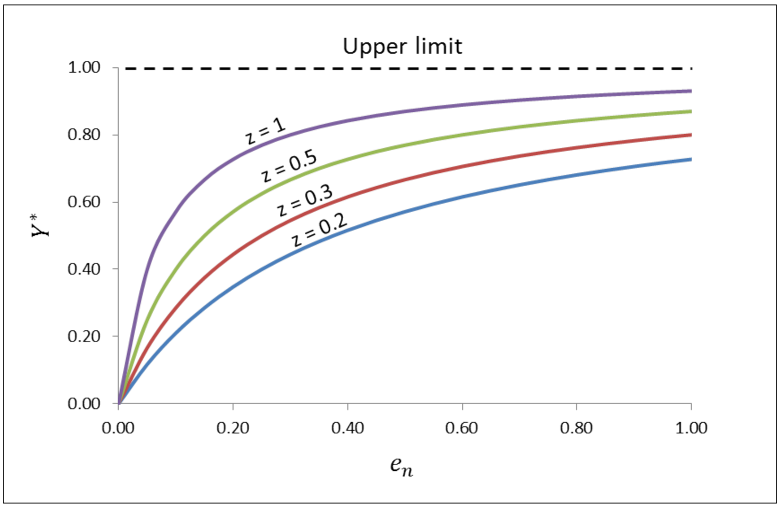

Figure 5.17: Graphical representation of Equation 5.8 showing the evaluation of Y^* with e_n for different z-values.

6. Conclusions

The basic conclusions that can be drawn from this investigation are the following:

It is confirmed that solid-state joining of dissimilar aluminum alloys can be performed using cold pressure welding (CPW). The two sets of alloy combinations in question are cold-deformed AA5183 and soft-annealed AA5183 (Series II) and cold-deformed AA5183 and commercial purity AA1050 (Series III). The results show that a minimum plastic deformation, corresponding to a nominal strain of 1.19 and 1.35, is required to initiate bonding in Series II and III, respectively. To achieve full bonding, nominal strains of 1.40 and 1.81 are required.

The successful joints reveal a weld zone thickness of roughly 0.3 mm with no sign of cracks or oxide present at the interface. In both series a normal deformation microstructure is observed, where the material flows in an outwards direction during upsetting forming flash when exiting the weld zone.

In Series II the soft material experiences a rapid increase in hardness within the weld zone, approaching that of the hard cold-deformed alloy. This is due to the characteristic strong work-hardening behavior of Al-Mg alloys. A slight increase in hardness of the hard alloy in the weld zone can also be observed.

In Series III the hardness gradient across the weld zone is incredibly steep, barely possible to resolve using micro-hardness measurements. In this case the hard alloy acts as a piston, penetrating the soft alloy, leading to a build-up of an internal extrusion pressure in the vicinity of the contact surface. At the same time the two alloys work-harden to a certain extent before the steep extrusion pressure gradient is established at the contact surface.

A dark demarcation line has been observed after joining of the two dissimilar aluminum alloys in Series III. This line is most likely traces of the cliff being established during simultaneous grinding and polishing of the two samples with highly different mechanical properties (i.e. hardness values).

The indications are that a much lower surface exposure is required to achieve metallic bonding in CPW than previously anticipated. This is probably due to a difference in the flow behavior between the softer bulk material and the harder interface material during upsetting. Obviously, the higher deformation resistance of the latter material will lead to a smaller value for the interface exposure compared to that calculated from simple measurements of the actual change of length of the cold pressure welded specimens.

References

[1] O.R. Myhr and Ø. Grong. "Process Modelling Applied to 6082-T6 Aluminium Weldments-I. Reaction Kinetics." In: *Acta Metallurgica et Materialia* (1991), pp. 2693–2702.

[2] O.R. Myhr and Ø. Grong. "Process Modelling Applied to 6082-T6 Aluminium Weldments-II. Applications of model." In: *Acta Metallurgica et Materialia* (1991), pp. 2703–2708.

[3] J.T. Desaguliers. "Some Experiments concerning the Cohesion of Lead, by the Same". In: *Phil. Trans.* 33 (1724), pp. 345–347.

[4] K. Mori et al. "Joining by plastic deformation." In: *CIRP Annals - Manufacturing Technology* 62 (2013), pp. 673–694.

[5] H.R. Madaah Hosseini and A.H. Kokabi. "Cold roll bonding of 5754-aluminium strips." In: *Materials Science and Engineering A* 335 (2002), pp. 186–90.

[6] N. Bay. "Mechanisms Producing Metallic Bonds in Cold Welding." In: *Welding Journal* 62 (1983), pp. 137–142.

[7] L. de Chiffre. *Method and tool for joining of metals or metal alloys by cold welding.* 1988. URL: `http://www.google.com/patents/WO1988000872A1?cl=en`.

[8] P. Dorph, L. de Chiffre, and N. Bay. "Experimental Analysis of Cut Welding in Aluminium." In: *CIRP Annals* 42 (1993), pp. 357–360.

[9] M. Rozmus and W. Rozmus. *Fine wire butt welder.* 1973. URL: `http://www.google.com/patents/US3768718`.

[10] BWE Ltd. May 2014. URL: `http://www.bwe.co.uk/`.

[11] ASM Handbook. *Welding, Brazing, and Soldering.* Vol. 6. ASM International, Materials Park, Ohio, 1993.

[12] W. Zhang and N. Bay. "A Numerical Model for Cold Welding of Metals." In: *CIRP Annals* 45 (1996), pp. 215–220.

[13] W. Zhang and N. Bay. "Cold Welding - Experimental Investigation of the Surface Preparation Methods." In: *Welding Journal Research Supplement* 76 (1997), pp. 326–330.

[14] A. Lilleby et al. "Experimental and Finite Element Studies of the Divergent Extrusion Process under Conditions Applicable to Cold Pressure Welding of Commercial Purity of Aluminium." In: *Materials Science and Engineering A* 518 (2009), pp. 76–83.

[15] A. Lilleby, Ø. Grong, and H. Hemmer. "Experimental and Finite Element Simulations of Cold Pressure Welding of Aluminium by Divergent Extrusion." In: *Materials Science and Engineering A* 527 (2009), pp. 179–186.

[16] A. Lilleby, Ø. Grong, and H. Hemmer. "Cold Pressure Welding of Severely Plastically Deformed Aluminium by Divergent Extrusion." In: *Materials Science and Engineering A* 527 (2010), pp. 1351–1360.

[17] E.A. Sandvik. *Cold pressure welding of corrosion resistant Al-Mg alloys.* Project work. Norwegian University of Science and Technology (NTNU), 2013.

[18] G.E. Dieter. *Mechanical Metallurgy.* SI Metric Edition. McGraw-Hill Book Company, London, 1988.

[19] A. Oosterkamp, L.D. Oosterkamp, and A. Nordeide. "'Kissing Bond' Phenomena in Solid-State Welds of Aluminum Alloys." In: *Welding Journal* 83 (2004), pp. 225–231.

[20] C. Leitão, A. Loureiro, and D.M. Rodrigues. *Influence of Base Material Properties and Process Parameters on Defect Formation during FSW.* International Congress on Advances in Welding Science and Technology for Construction, Energy & Transportation Systems (AWST 2011), 2011.

[21] K. Krog et al. *Experimental studies of the bonding mechanisms in cold pressure welded aluminium joints (in Norwegian).* Technical Rapport STF80MK F06361. SINTEF, 2006.

Appendix

A. Soft-annealing experiments

Below is a collection of micrographs covering the whole temperature range of the recrystallization process in the AA5183 alloy during soft-annealing.

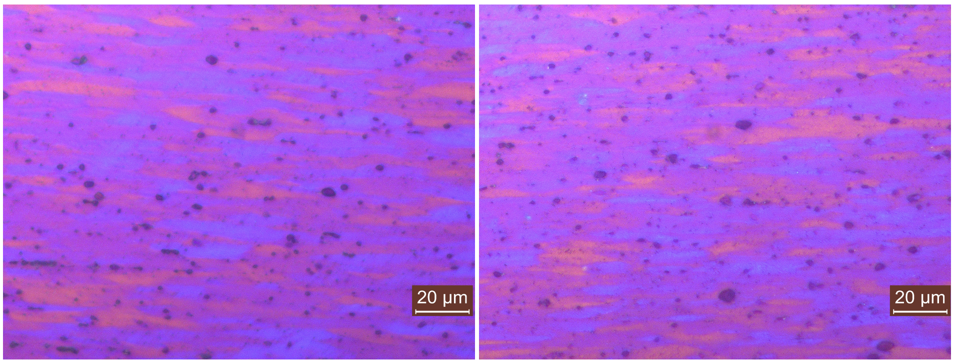

(a) RT (b) 100°C

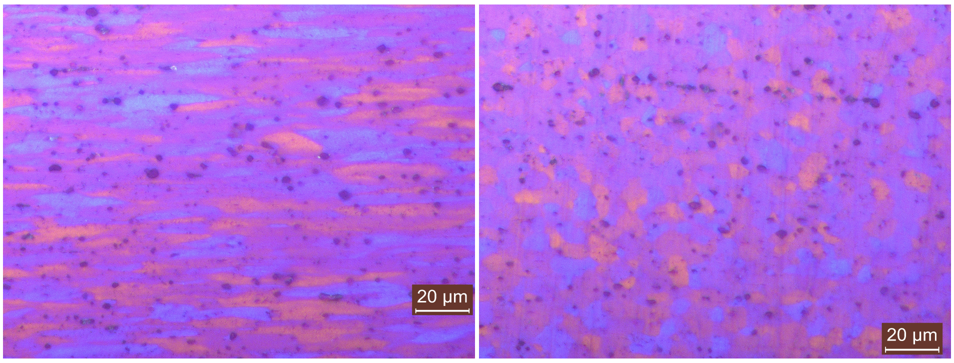

(c) 200°C (d) 300°C

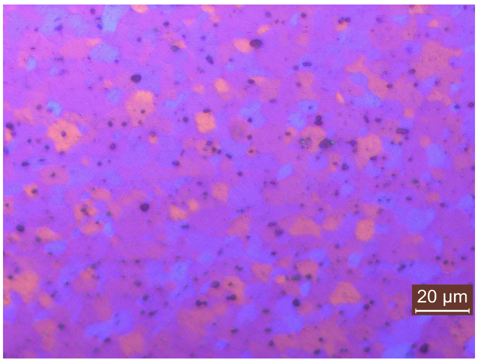

(e) 400°C

Figure A.1: Optical microscope pictures of the microstructure of AA5183 (a) before heat treatment (b) after heat treatment at 100°C (c) after heat treatment at 200°C (d) after heat treatment at 300°C (e) after heat treatment at 400°C.